

Seismic Performance of Deposit Slopes With Underlying Bedrock Before and After Reinforcement by Stabilising Piles

Zhiliang Sun (✉ zlsun@whrsm.ac.cn)

Wuhan Institute of Rock and Soil Mechanics Chinese Academy of Sciences <https://orcid.org/0000-0002-2330-7908>

Kong Lingwei

Wuhan Institute of Rock and Soil Mechanics Chinese Academy of Sciences

Bai Wei

Wuhan Institute of Rock and Soil Mechanics Chinese Academy of Sciences

Wang Yong

Wuhan Institute of Rock and Soil Mechanics Chinese Academy of Sciences

Research Article

Keywords: rock-soil mixture deposit, slopes, stabilising piles, centrifuge models, seismic response

Posted Date: March 19th, 2021

DOI: <https://doi.org/10.21203/rs.3.rs-327893/v1>

License:   This work is licensed under a Creative Commons Attribution 4.0 International License.

[Read Full License](#)

1 Seismic performance of deposit slopes with underlying bedrock before and after reinforcement by
2 stabilising piles

3 Sun Zhiliang ^{a,b,*}, Kong Lingwei ^{a,b}, Bai Wei ^{a,b}, Wang Yong ^{a,b}

4 a. State Key Laboratory of Geomechanics and Geotechnical Engineering, Institute of Rock and Soil
5 Mechanics, Chinese Academy of Sciences, Wuhan, Hubei 430071, China

6 b. University of Chinese Academy of Sciences, Beijing, 100049, China

7 *Corresponding author.

8 E-mail addresses: zlsun@whrsm.ac.cn (Sun Zhiliang), lwkong@whrsm.ac.cn (Kong Lingwei),
9 wbai@whrsm.ac.cn (Bai Wei), wang831yong@163.com (Wang Yong)

10
11 Abstract: The seismic performance of stabilising piles used to reinforce underlying bedrock in a deposit
12 slope is a complex soil-structure interaction problem, on which there is limited design guidance on the
13 optimum use of a single row of rock-socketed piles to reinforce such slopes. Two centrifuge
14 shaking-table model tests at a geometric scale of 1:50 were conducted to ascertain the dynamic
15 responses of the underlying bedrock deposit slopes without and with the use of stabilising piles during
16 an earthquake. Multi-stage seismic waves with various peak accelerations were applied from the
17 bottom of each model. Under seismic excitation, the differences in the response accelerations between
18 the deposit and bedrock increase significantly with the increase in amplitude of the input seismic waves.
19 The two are prone to uncoordinated movement, which leads to slope instability. Setting stabilising piles
20 reduces the crest settlement and angular deformation and changes the natural frequency of the slope
21 crest. The presence of the rock-socketed stabilising piles can bridge the uncoordinated movement of the
22 bedrock and the overlying deposit to some extent. According to the mobilised pile bending moment,
23 shear force, lateral pile-soil load distribution, and pile displacement, the dynamic response
24 characteristics of stabilising piles under continuous multi-level seismic excitation were analysed. The
25 resultant force arising from a distributed load increment on the piles caused by an earthquake is mainly
26 concentrated in the upper part (the point of action of the resultant force is 1.54m below the slope
27 surface). With increases in the peak ground acceleration (PGA) of the input motion, the resistance of
28 the bedrock in front of the stabilising piles increases; moreover, with the increase of PGA, the peak
29 resistance under the bedrock surface of the stabilising piles gradually moves downwards. This finding
30 indicates that the strong seismic motion significantly changes the embedded working state of the
31 stabilising pile.

32 Key words: rock-soil mixture deposit; slopes; stabilising piles; centrifuge models; seismic response.

33
34 1 Introduction

35 Mixed rock and soil deposits mainly stem from landslide accumulation, residual accumulation, alluvial
36 accumulation, *etc.* and are distributed widely as large-scale slopes in Sichuan Province, China (Huang
37 and Li 2009; Ding *et al.* 2012). Deposit collapse and landslides account for a significant proportion of
38 the disasters caused by the Wenchuan earthquake (Chigira *et al.* 2010; Cao *et al.* 2011; Yin *et al.* 2009).
39 Theoretical analysis and research have shown that the surface amplification effect of a seismic slope is
40 closely related to the impedance difference and wave velocity difference of near-surface geo-materials
41 (Massey *et al.* 2017; Bourdeau *et al.* 2008; Del Gaudio and Wasowski 2011), such as the overlying
42 deposit (filling layer, colluvium layer, alluvium layer, *etc.*) on the bedrock, and the strong weathering

43 layer covering the weak weathering layer, *etc.* (Strenk and Wartman 2011; Moor *et al.* 2011; Gischig *et*
44 *al.* 2015). Deposit slopes with underlying bedrock are prone to secondary disasters such as dammed
45 lakes and mudslides. In recent years, the construction of large-scale water conservancy projects,
46 hydropower projects, and transportation hubs in south-western China have been undertaken and the
47 risk of huge loss of life and property caused by earthquakes is increasing.

48 Stabilising piles are one of the most widely used engineering structures in landslide management
49 because of the small disturbance of the surrounding geological environment, good support effect, and
50 ease of construction (Carder and Temporal 2000; Li and Pei 2012; Lirer 2012; Li *et al.* 2016). On the
51 other hand, the disaster investigation teams deployed after the Wenchuan earthquake found that
52 stabilising piles generally had a good anti-seismic effect, but there are also a large number of stabilising
53 piles that had overturned and even cracked and been broken (Wu *et al.* 2009). This suggests that the
54 current understanding of the anti-seismic mechanism of stabilising piles is not yet clear: design and
55 theory lag practical application and remain to be explored.

56 To understand the seismic strengthening mechanism of slope-stabilising piles, it is necessary to
57 clarify the dynamic response of slopes under seismic action, the distribution of stabilising pile bending
58 moment, and the distribution of earth pressures there on. At present, the research methods deployed
59 include: on-site monitoring (Smethurst and Powrie 2007; Huang and Li 2009; Spence 2015; Bonilla
60 2002; Ou *et al.* 2019) and model testing (Yu *et al.* 2010; Al-Defae and Knappett 2014, 2015; Wang and
61 Zhang 2014; Li *et al.* 2016; Ma *et al.* 2019; Huang *et al.* 2020). In recent years, there are more
62 numerical simulation data available from studies of slopes reinforced by stabilising piles (Ellis *et*
63 *al.* 2010; Sharafi and Shams 2019; Won *et al.* 2005; Erfani Joorabchi *et al.* 2014; Kanagasabai *et al.*
64 2011; Kourkoulis *et al.* 2011), however, most of these studies are focussed on the behaviour of
65 homogeneous slopes reinforced by stabilising piles.

66 The dynamic centrifuge model test can be used to simulate the prototype self-weight stress and
67 replicate *in-situ* stress conditions. The test results can be used to verify the reliability of a numerical
68 simulation; because of its operability and repeatability, it is an important technique in research into the
69 effects of seismicity on slopes. From the perspective of the interaction between homogeneous sand and
70 a pile, the former studies mainly focus on the seismic response characteristics of slope reinforced by
71 stabilising piles (Al-Defae and Knappett 2014, 2015; Yu *et al.* 2010), the seismic response
72 characteristics of inclined pile foundations (Li *et al.* 2016), and the influence of liquefaction on pile
73 foundations through centrifugal shaking-table model tests (Abdoun *et al.* 2003; Brandenberg *et al.*
74 2005; Knappett and Madabhushi 2009), *inter alia*. From the perspective of the interaction between
75 homogeneous clay and a pile, Wang and Zhang (2014) conducted centrifuge model tests to study the
76 seismic strengthening mechanism of stabilising piles by assessing the deformation profiles of slopes
77 reinforced by stabilising piles under seismic load. Garala and Madabhushi (2019) studied the
78 interaction between friction piles and soft clay under seismic load in centrifuge model tests. The
79 aforementioned dynamic model tests of slope stabilising piles, and their mechanism of action, are
80 mainly based on the dynamic response characteristics of sand, clay, and other homogeneous slopes;
81 however, there are few studies on the dynamic response of a deposit slope with underlying bedrock and
82 the working mechanism of the coarse-grained rock and soil mixture deposits, thus making it difficult to
83 meet the needs of engineering practice.

84 Therefore, in this research, two sets of centrifuge shaking-table model tests were conducted to study
85 the seismic response of a deposit slope with underlying bedrock with stabilising pile reinforcement and
86 a similar unreinforced slope. The distributions of bending moments and lateral pile-soil load under

87 continuous multi-level seismic loading were further explored. In the present work, the results are
88 presented in terms of prototype-scale.

89 2 Centrifuge testing programme

90 2.1 Test instrumentation

91 The testing facilities included a ZJU-400 centrifuge and an electro-hydraulic servo-controlled shaking
92 table developed by staff at Zhejiang University, China. It has an effective radius of 4.50 m and a
93 capacity of 400g-tons. The size of the shaking table used in the tests is 800mm in length and 600mm in
94 width. Its loading capacity is 0.5 ton. The seismic waves were applied to the model in the horizontal
95 direction through the shaking table, which had a maximum acceleration capacity of 40g (Chen *et al.*
96 2017; Zhou *et al.* 2018). The advantage of the centrifuge is that it allows the use of reduced-scale
97 models to realise full-scale stress conditions. A rectangular rigid model box with internal dimensions of
98 770mm × 400mm × 530mm (length× width× height) was used. A layer of soft plasticine plate with a
99 thickness of 25 mm was sandwiched between the deposit and each end-wall. This set-up was used to
100 absorb energy and reduce the intensity of reflected waves at the boundaries in the shaking direction
101 (Sun *et al.* 2019).

102 2.2 Similarity relationship and slope model design

103 The similarity scale of the slope model is 50 (prototype size / model size = 50), and the similar
104 relationship of the centrifuge model is summarised in Table 1. In the present work, the model is
105 somewhat idealised. The model is intended for use as a generic study of the seismic response
106 mechanism rather than to represent a specific prototype. Fig.1 shows the schematic views of the
107 unreinforced slope model (1[#]model), pile reinforced slope model (2[#]model), and model piles used for
108 the primary test. The geometry of the unreinforced slope is identical to that of the pile-reinforced
109 model.

110 Stabilising piles in the 2[#]model were made of aluminium alloy hollow square tube, with a side length
111 of 30mm and a thickness of 1.8mm. The pile spacing is $4b$, namely $S=120$ mm. The parameters
112 pertaining to the prototype stabilising pile are listed in Table 2. According to Kourkoulis *et al.* (2011,
113 2012), the pile embedment depth $L_e \geq 0.7H_u$ (L_e is the pile embedment length and H_u is the depth of the
114 unstable soil layer) can guarantee working stability when the pile is embedded in a stronger substratum.
115 In 2[#]model in Fig.1(b), L_e/H_u is nearly 0.61.

116 2.3 Soil properties

117 Deposit samples were collected from the Mianmao Highway line, Sichuan Province. The sampled
118 material has a small fines content, a mean grain size d_{50} of 3.3mm, a uniformity coefficient C_u of 9.95,
119 and a curvature coefficient C_c of 1.70. The particle size distribution characteristics of the tested deposit
120 are listed in Table 3. The minimum and maximum void ratios (e_{\min} and e_{\max}) are 1.466 and 2.102,
121 respectively. The internal friction angle of the tested deposit is 41° and its apparent cohesion is 4.8 kPa
122 at a relative density of 0.628, and an initial dry density of 1.81 g/cm³.

123 2.4 Model preparation and test procedure

124 The cemented material was used at a compacted density of 1.92 g/cm³ when used to represent the
125 bedrock. The mass percentage composition of the cemented material was silica sand: fines fraction of
126 deposit: cement: water = 1: 1: 0.34: 0.27, and rapid strengthening agents were added to 2% mass of the
127 cement. Then the constructed bedrock model was cured for six days and the dynamic centrifuge tests
128 were performed on day 7. The friction angle was 44° and cohesion was 201 kPa for the cemented
129 material after a 7-day curing period as evinced by direct shear test data. The interface between the
130 bedrock and deposit was generalised as two inclined planes and a horizontal plane, with inclined plane

131 angles of 45° and 20°, respectively (Figs 1(a) and 1(b)).

132 Pile bending moments were measured by seven pairs of strain gauges in a full bridge configuration
133 mounted on the tube surface (Fig.1(c)): lateral pile-soil pressures were measured by four miniature
134 transducers embedded in the pile. Pile strain gauges and miniature earth pressure transducers were
135 calibrated before installation. After calibration and verification that all sensors were working, the model
136 piles were then embedded in the bedrock.

137 When preparing the upper layer of the slope models, the deposit materials were compacted after
138 placement in the model box using the controlled-volume method (Wang and Lin 2011) to a dry density
139 of 1.81g/cm³. After placement of each layer, the deposit surface was smoothed with a soft brush and
140 instruments were placed in their specific positions. Silicone oil was smeared over the sides of the rigid
141 box to provide a lower friction coefficient at the interface with the walls.

142 The dynamic input was provided by the shaking table in the centrifuge. Multiple shaking events (El
143 Centro motion) covering a wide range of peak ground accelerations(PGA) were applied to both the 1[#]
144 and 2[#] models while in flight. The shaking was applied parallel to the long sides of the model container
145 and orthogonal to the pile row. The peak values of the horizontal input acceleration in the shaking
146 events were adjusted to nearly 0.05g, 0.10g, 0.20g, 0.40g, and 0.20g at prototype-scale (corresponding
147 to 2.5g, 5.0g, 1.0g, 2.0g, and 1.0g at model-scale), which corresponded to seismic intensities of 6°, 7°,
148 8°, 9°, and 8° based on the “Code for Seismic Design of Buildings” in China (GB 50011-2010). The
149 time histories of input motions at instrument BA-0 are shown in Fig.2.

150 3 Acceleration response and crest settlement of slope

151 3.1 Horizontal response acceleration

152 The PGA amplification factor S_p is defined as the peak acceleration at a given depth normalised to the
153 peak acceleration of the input motion) in the centrifuge tests as a function of normalised elevation
154 (h/H).

155 (1) Unreinforced slope

156 Fig.3 shows that, before reinforcement using stabilising piles, the PGA amplification factor of the slope
157 increases substantially along the elevation direction and reaches the maximum at the crest of the slope.
158 Under the continuous application of five levels of seismic load, the PGA amplification factor at the
159 crest of the slope (A-3) has a mean average value of about 1.97, thus exacerbating the elevation
160 amplification effect.

161 Moreover, at the same elevation on the slope, the PGA amplification factor of the deposit surface is
162 greater than that of the bedrock surface, as shown in Fig.3(a), BA-0→A-144→A-179 and in Fig. 3(b),
163 BA-0→A-2→A-6→A-4. For example, at the height of 15.8m (A-4, A-142, A-179), the horizontal
164 acceleration amplification factor distribution from the inside of the slope to the surface of the slope is
165 illustrated in Fig.4. The mean average acceleration amplification factors from within to the surface are
166 1.10, 1.06, and 1.27, respectively. The difference of the PGA amplification factors between deposit
167 surface and bedrock surface shows typical surface amplification.

168 The strength difference of the bedrock and deposit also affects the seismic amplification effect. The
169 shear strength of the deposit is lower than that of the bedrock, and the PGA amplification factors in that
170 deposit are greater than those in bedrock. Acceleration sensors A-2, A-6, and A-4 are placed in the
171 bedrock, as shown in Fig.3(b), and the measured amplification factors are close to 1.0.

172 Fig.5 shows the transfer coefficient from A-0 to A-3: the components at frequencies of about 5 to
173 7Hz are amplified when the seismic wave propagates from the bottom to the crest of the slope in the
174 1[#]model.

175 (2) Slope reinforced by a discretely spaced pile row

176 Fig.6 shows the distribution of response accelerations along the slope elevation when reinforced by
177 stabilising piles. It also shows increased amplification and surface amplification as compared in Figs
178 6(a) and 6(b). As shown in Fig.6(a), the average PGA amplification factor obtained from the crest
179 measuring point (A-1) under continuous application of five levels of load is about 1.42, which is less
180 than that obtained from A-3 (1.97) in Fig.4(a) when the slope is not reinforced by stabilising piles.

181 It is worth noting that the difference in PGA amplification factors between A-3 and A-144 is
182 significant in the 2[#]model, as shown in Fig.6(a). The accelerations measured at A-144 and A-139,
183 located below the stabilising piles, were significantly suppressed, while the acceleration measured at
184 A-3 and A-7, located above the stabilising piles, increased slightly. A possible reason for this is that the
185 stabilising piles lead to greater superposition of wave reflections in the passive zone under such seismic
186 excitation, which generally shows that the amplification effect of horizontal response accelerations
187 increases in front of the stabilising piles and decreases below them.

188 The horizontal acceleration amplification factor distribution from the interior of the slope to its
189 surface at a height of 15.8m in the 2[#]model during centrifuge testing is as shown in Fig.7. Akin to Fig.4,
190 Fig.7 also shows the effect of surface amplification. The mean average acceleration amplification
191 factors under each of the five levels of seismic load from the inside to the surface are 1.05 (A-4), 1.14
192 (A-179), and 1.29 (A-7), respectively.

193 Fig.8 shows the amplitude ratios of the transfer function of the acceleration measured at A-1(slope
194 crest) and A-0 (bottom of the model box) in the 2[#]model during centrifuge testing. In addition to the
195 frequency components at 5 to 7Hz, the frequency components at 15 to 17Hz are also significantly
196 amplified as the seismic wave propagates from the bottom to the crest, and the amplification is even
197 greater than that of components at 5 to 7Hz.

198 (3) Comparison between unreinforced and reinforced slopes

199 Comparing Figs 5 and 8, the spectrum amplification effect of the input seismic wave is changed
200 significantly after the landslide is reinforced by stabilising piles. This shows that the resonance
201 frequency of the slope system is shifted from 5-7Hz to 15-17Hz after the stabilising piles has been
202 installed.

203 To facilitate the analysis of the trend in the acceleration amplification effect inside the slope, the
204 mean average value of the PGA amplification factors under multiple sequential ground motions was
205 adopted at each measuring point, as shown in Fig.9.

206 From Fig.9(a), the mean average acceleration amplification factor in the upper part of the slope
207 (A-179) is 1.326, which is greater than the magnification (A-4) at the same elevation within the slope
208 (only slightly greater than 1), therefore, the different behaviours of the exterior and the interior of the
209 slope will induce non-uniform movement. Qualitatively, the seismic waves that are transmitted from
210 within the slope form superimposed reflection and interference effects on the superficial layer, resulting
211 in an acceleration amplification factor of the slope surface that is larger than that within the slope.
212 Comparing Fig.9(a) with Fig.9(b), it can be found that after the stabilising piles are installed, the
213 acceleration amplification factor near the slope surface is reduced compared with that beforehand.
214 Stabilising piles bridge the difference of acceleration response between the bedrock and deposit. The
215 reason for the surface amplification effect can be explained as follows: part of the seismic energy is
216 dissipated by damping during the propagation of seismic waves in the rock and soil mass, while the
217 remaining energy is manifest as the seismic response of the rock and soil mass. The bedrock of the
218 slope is harder than the upper part, so more energy is dissipated therein, and the dynamic response is

219 smaller, while the surface soil mass of the slope is loose, the dynamic response is greater (Huang 2009;
220 Massey *et al.* 2017). The inconsistency of the acceleration amplification effect will lead to an
221 inconsistency of movement between the slope surface and the deep layer. The uncoordinated movement
222 between the shallow soil and the rock in the slope produces a stripping tensile stress, and finally leads
223 to the formation of a shallow surface landslide.

224 Fig.10 shows that the amplitude of the slope crest acceleration response spectrum (ARS) is
225 decreased significantly after installing a single row of stabilising piles as reinforcement ($S/b=4$) to the
226 underlying bedrock deposit slope. In shaking event EQ4, the response spectrum values in the frequency
227 range shown in Fig.10 are significantly reduced after the stabilising piles are installed, and the
228 amplitude of the ARS decreases by 37%. Overall, the larger the PGA of the input motion, the more
229 significant the effect of the stabilising piles on the ARS peak reduction.

230 3.2 Crest settlements

231 The permanent crest settlements in each shaking event were monitored by laser displacement
232 transducers LDS-1 and LDS-2 (Fig.1). The time-history curves of the slope crest settlements of each
233 shaking event in the 1[#] and 2[#] models are shown in Fig.11.

234 The permanent displacement of slope crest occurs only when the acceleration amplitude of the input
235 ground motion reaches a threshold, and Newmark (1965) defined it as the critical acceleration. As
236 shown in Fig.11, the crest settlements increased with increasing input amplitude of ground motions. In
237 the shaking events EQ1 and EQ2, no obvious settlement occurred in the two models. When the input
238 amplitude exceeded 0.2g in shaking event EQ3, significant plastic deformation occurs in the slope crest
239 as measured at LDS-2 in both models. In shaking event EQ4 in the 1[#] model, $\Delta_{d1}=17.1$ mm and
240 $\Delta_{d2}=178.2$ mm, after stabilising piles are installed; $\Delta_{d1}=12.4$ mm and $\Delta_{d2}=121.1$ mm in the 2[#] model,
241 and the crest settlements are reduced by approximately 27% and 32%, respectively. The piles would be
242 expected to increase Newmark's yield acceleration, as described by Al-Defae and Knappett (2013).

243 The distance ΔL between LDS-1 and LDS-2 is 3 m in the prototype and the angular rotation of the
244 slope crest during the test is defined as follows: $\tan\Delta\theta = (LDS2 - LDS1) / \Delta L$, where LDS2 and LDS1
245 refer to the values measured by using laser displacement transducers LDS-2 and LDS-1. The
246 time-history curve of crest angular rotation is also shown in Fig.11. The final cumulative angular
247 deformation in the 1[#] model is 0.06rad (3.4°), and that in the 2[#] model is 0.0425rad (2.4°). The change
248 in angular rotation at the crest is almost the same as that in the crest settlement, which indicates that the
249 crest settlement and the angular rotation will occur at the same time.

250 4 Response characteristics of stabilising piles under seismic load

251 4.1 Horizontal displacement

252 Fig.12 shows the time-history curve of the pile top horizontal displacement measured by laser
253 displacement transducer LDS-3 in the centrifuge shaking table model test. The trend in pile top
254 horizontal displacements in Fig.12 is akin to that in Fig.11: under a small input ground motion (EQ1,
255 EQ2), there is almost no residual horizontal displacement at the pile top. In shaking event EQ3
256 (PGA=0.236g), the residual horizontal displacement of the pile top begins to occur, indicating that the
257 stabilising piles begin to be pushed, so that the pile top starts to undergo horizontal residual
258 deformation. Under the excitation of a strong earthquake (EQ4, PGA = 0.421g), the pile top undergoes
259 a significant horizontal displacement, in which the maximum instantaneous horizontal displacement
260 reaches 15.8 mm and the residual horizontal displacement of the pile top is 6.7 mm. This shows that the
261 overlying deposits have a sliding, downwards trend, and the stabilising piles have begun to bend
262 significantly. From EQ4 to EQ5, the incremental residual horizontal displacement of the pile top is

263 minimal, suggesting that the previous vibration has enhanced the seismic resistance of the slope to
264 some extent when the slope is subjected to a strong excitation first and then excited by a smaller
265 earthquake.

266 Fig.13 shows the amplitude ratios of the transfer function of the acceleration measured at A-1079
267 (pile top) and A-0 (bottom of the model box) in the 2[#] model during centrifuge testing. Its distribution is
268 similar to that in Fig.8. The difference is that the amplification factor of frequency components at 5 to 7
269 Hz at the top of stabilising piles is greater than that at the crest of the slope in the 2[#] model.

270 4.2 Bending moment

271 The typical response time-history curve of bending moments in the centrifuge model test (EQ4, S3)
272 is shown in Fig.14. The residual bending moment increment ΔM_r in each shaking event is defined as
273 the difference between the beginning and the end of the response time-history curve of the bending
274 moment. During the seismic loading process, the maximum dynamic bending moment M_{\max} and the
275 minimum dynamic bending moment M_{\min} in each shaking event are taken as the difference between the
276 beginning and the peak and trough of the time-history curve of the bending moment, respectively.

277 Fig.15 shows the time-history curves of bending moments measured by strain gauges on a stabilising
278 pile under five continuous earthquake excitations (only 6s of the time-history are taken in each case to
279 show the variation in the bending moment). It can be seen from Fig.15 that the bending moment
280 measured at different points on the stabilising piles does not reach the maximum value at the same time.
281 Taking EQ3 as an example (Fig.15(c)), the corresponding times to the peak signal amplitude are
282 109.91s, 109.91s, 109.92s, 109.93s, 109.95s, and 110.03s (S1-S7), and the corresponding times to the
283 wave trough are 109.35s, 109.35s, 109.36s, 109.37s, 109.38s, 109.37 s, and 109.48s (S1-S7) at each
284 strain gauge. It can be seen that the bending moment on the stabilising piles embedded in bedrock (S1,
285 S2, and S3) exhibits no phase difference, while there is a phase difference in the bending moment on
286 the pile above the bedrock (S4, S5, S6, and S7), especially near the top of the pile (S7) where the time
287 difference is about 0.1s. This is mainly due to the interaction between the stabilising piles and the
288 deposit, and the onset of the effect of viscous damping which will be beneficial to the dissipation of
289 earthquake energy.

290 The bending moment corresponding to the characteristic time shown in Fig.15 is extracted.
291 Meanwhile, the maximum and minimum bending moments generated during the earthquake (due to the
292 phase difference, the bending moment at each measurement point on the stabilizing pile cannot reach a
293 maximum or minimum at the same time, which is called the maximum or minimum bending moment
294 envelope) and the residual bending moment after the earthquake is extracted. After deducting the initial
295 static bending moment generated by centripetal acceleration before the earthquake, the bending
296 moment diagram along the pile height is plotted in Fig.16.

297 It can be seen from Fig.16 that the dynamic bending moment corresponding to each characteristic
298 time changes within the envelopes of the maximum and minimum dynamic bending moments.
299 Therefore, the envelopes of maximum and minimum dynamic moments can be used as a basis to
300 determine the design load in the seismic design of a stabilising pile. When the input seismic load is
301 relatively small (EQ1, PGA=0.055g; EQ2, PGA=0.125), the positive and negative dynamic bending
302 moments of the pile are quasi-symmetrically distributed, and the residual bending moment after the
303 earthquake is small (and even negligible in EQ1) (Fig. 16 (a)).

304 After each shaking event (Figs 16(a)-(c)), the distribution of residual bending moment along the
305 instrumented pile gradually increases from the slope surface to the bedrock surface, then decreases
306 from the bedrock surface to the pile bottom, showing an outward convex shape, that is, the position of

307 the maximum residual bending moment is near the bedrock surface, which is related to the earth
 308 pressure acting on the stabilising piles. After seismic loading at PGA=0.125g, the residual bending
 309 moment along the instrumented pile begins to increase, indicating that the overlying deposit begins to
 310 slide under the influence of the ground motion, which is consistent with the phenomenon whereby the
 311 aforementioned slope crest settlement starts to occur in shaking event EQ2 (Fig.11(b)).

312 In the first three shaking events (EQ1, PGA=0.055g; EQ2, PGA=0.125g; EQ3, PGA = 0.236g), the
 313 peak value of dynamic bending moment appears at measurement point S3 ($H = 5.5\text{m}$), that is to say, it
 314 reaches its peak value near the bedrock-deposit interface: however, in EQ4 (PGA=0.421g), the positive
 315 maximum dynamic bending moment is still located at S3 at $t = 159.19\text{s}$, and the bending moment
 316 measured at S2 rapidly approaches that at S3 at $t=159.97\text{s}$. At $t=161.84\text{s}$, the positive bending moment
 317 at S2 has exceeded that at S3, that is, the positive maximum dynamic bending moment is located at S2
 318 ($H = 3.5\text{m}$). The residual bending moment after earthquake EQ4 and the maximum positive dynamic
 319 bending in EQ5 are finally located at S2 ($H = 3.5\text{m}$) (Figs 16(d) and (e)). This shows that, under strong
 320 earthquake excitations, the part of the bedrock surface behind the stabilising piles begins to yield, the
 321 bearing layer of the bedrock socketed section moves down, as depicted in Fig.17, indicating that the
 322 strong seismic loading has significantly changed the stress state in the embedded section of the pile. It
 323 can be foreseen that, when the seismic load is further increased and the overturning moment generated
 324 by the landslide body exceeds the stabilising moment provided by the bearing capacity of the bedrock,
 325 the stabilising piles will undergo tilting-overturning failure.

326 It can be seen from Figs 16(d) and (e) that, if the model slope has experienced strong ground motion
 327 (e.g., EQ4, PGA=0.421g) beforehand, when the slope experiences a smaller earthquake motion (e.g.,
 328 EQ5, PGA=0.236g) thereafter, the residual bending moment on the stabilising piles is almost
 329 unchanged. When continuous five-level excitation is applied, the maximum residual bending moment
 330 approaches 3250 kN·m. That is, the seismic load causes the overlying deposit to slide, and the
 331 permanent thrust generated on the stabilising piles increases the maximum bending moment by 3250
 332 kN·m.

333 4.3 Lateral pile-soil load

334 In the dynamic centripetal modelling tests, four earth pressure cells were placed on the stabilising pile
 335 above the bedrock surface. Fig.18 shows the incremental earth pressure measured after each shaking
 336 event. In addition, according to the differential relationship between moment M , shear force Q , and

337 distributed load q on the stabilising pile ($\frac{dM}{dx} = Q, \frac{dQ}{dx} = q$), the distributed load q on the stabilising pile

338 after each shaking event can be roughly obtained ($\frac{\Delta M}{\Delta h} = \bar{Q}, \frac{\Delta \bar{Q}}{\Delta h} = \bar{q}$, where Δh is the distance

339 between two adjacent moment gauges) from the residual moment diagram in Fig. 16. The comparison
 340 of distributed load increment obtained by moment strain gauge and earth pressure cell (from pressure
 341 integral to distributed load) on a stabilising pile after each shaking event is shown in Fig. 19 (the
 342 increment of distributed load in EQ1 is almost zero, so is not shown in Fig. 19 for clarity). It should be
 343 pointed out that the centrifuge model test gave values of pile-soil pressure on only one side surface of
 344 the pile, while the distributed load calculated from the bending moment is the pressure transmitted by
 345 the soil to the whole pile (four surfaces). There are differences between the two: Fig.19 shows that the
 346 distributions of the two are similar, but the values differ significantly when increasing the input PGA.

347 To verify the rationality of the aforementioned differential method, Fig.20 shows the simplified
 348 distributed load increment above the slip surface after each shaking event according to Fig.19: the

349 shape of the distributed load increment is the same, but the magnitude increases gradually with the
350 increase of the input PGA.

351 The increment of distributed load in EQ1 is almost zero and in EQ5 it is equal to that in EQ4. It is
352 noted that the distributed load increment generated by the seismic excitation in Fig.20 is negative near
353 the slip surface, which indicates that the earth pressure in front of the pile is large, and the sliding force
354 generated by the seismic excitation is mainly concentrated in the part above 3.5m up the slip surface. It
355 can be calculated that the point of action of the resultant force is 7.46m above the slip surface. The
356 point of action of the resultant force is 1.54m below the slope surface, which indicates that the
357 earthquake mainly causes shallow sliding of the deposit, resulting in distribution of the load increment
358 in the upper part of the pile.

359 Taking the simplified distributed load generated by the earthquake in Fig.20 as the external load, the
360 Mohr-Coulomb model was adopted for the bedrock (with the Young's modulus of bedrock set to 5.42
361 GPa, and Poisson's ratio to 0.30), and the stabilising pile (Table 2) was simulated as a Mindlin beam
362 (Bathe 1982) with the help of PLAXIS 2D software (2015), the horizontal displacement, shear force,
363 and bending moment on a stabilising pile after an earthquake can be obtained (Fig.21). In Fig.21(a), the
364 horizontal displacements of pile in each shaking event are obtained by invoking Mindlin beam theory.
365 The horizontal displacements of the pile top from EQ2 to EQ5 are 0.601mm, 2.08mm, 8.88mm, and
366 8.88mm, respectively. The pile top horizontal displacements measured by laser displacement transducer
367 LDS-3 are 0.31mm, 1.48mm, 6.85mm, and 6.85mm, respectively. It can be found that the horizontal
368 displacement of the pile tip obtained by use of Mindlin beam theory is slightly greater than that
369 measured by laser displacement transducer, but the trend of the two is consistent. It can be seen from
370 Figs 21(b) and (c) that, when the input PGA is small (EQ2), the pile shear force and bending moment
371 obtained from Mindlin beam theory are in good agreement with the results obtained from the actual
372 conversion of experimental bending moment data. With the increase of PGA (EQ3 and EQ4) of the
373 input seismic wave, the shear force and bending moment on the pile in the bedrock obtained by
374 Mindlin beam theory are much greater than those obtained experimentally; this is because the
375 attenuation of the strength of the bedrock in front of the rock-socketed pile is not considered in the
376 theoretical calculations. It is confirmed again that the resistance of the bedrock in front of the pile is
377 redistributed under strong earthquake excitation (Fig.17). At the same time, it is verified that the
378 distribution of pile-soil load estimated by use of the differential method is reasonable (Fig.20) in this
379 case.

380 5 Conclusion

381 Under seismic excitation, the horizontal response accelerations in the two slopes show typical effects of
382 elevation amplifications, surface amplification, and lithology. The arrangement of stabilising piles
383 suppressed the downward trend in the motion of the overlying deposit. This results in a decrease in the
384 difference between internal accelerations and external accelerations of the bedrock at the same
385 elevation within the slope. A more obvious wave reflection superposition effect in the passive zone
386 caused by the piles under ground shaking leads to the slope surface PGA amplification factor
387 increasing in front of the piles and decreasing below the piles. In addition, through the transfer function
388 between the slope bottom and the slope crest accelerations, it can be found that the installation of
389 stabilising piles significantly amplified the 15 to 17Hz frequency component.

390 The permanent settlements and angular rotation of the stabilising-pile-reinforced slope crest are
391 reduced by about 30% compared with the unreinforced slope after five-stage seismic excitation is
392 applied in centrifuge tests. The installed piles will increase the Newmark yield acceleration of the

393 underlying bedrock deposit slope. The horizontal displacement at the top of the stabilising pile is
394 closely related to the slope crest settlement and angular deformation.

395 The bending moment at each point on the pile does not reach its maximum simultaneously. There is
396 a significant phase difference in the bending moment time-history curve pertaining to each
397 measurement point, and the bending moment at the pile top lags that at the pile bottom. The short-term
398 response amplitude of the dynamic bending moment is significantly larger than the corresponding
399 post-earthquake permanent residual bending moment. The lateral pile-soil pressure above the bedrock
400 gradually increases under continuous excitation imposed by five successive earthquakes. The point of
401 action of the distributed load (when expressed as a single resultant force) is 7.46m above the sliding
402 surface, indicating that the earthquake mainly causes shallow sliding of the deposit to produce a
403 residual sliding force. Under strong seismic excitation, the main bearing stratum of the pile-socketed
404 bedrock section moves downwards, indicating that the stress state in that section of the pile embedded
405 in the bedrock changes. In seismic design terms, the rock-socketed depth of each stabilising pile should
406 be carefully selected in such deposit slopes with underlying bedrock.

407

408 Acknowledgments

409 The study is supported by the National Key R&D Program of China (Grant No.2018YFC1505304), the
410 National Natural Science Foundation of China (Grant Nos. 41702348, 51979269), and the Hubei
411 Provincial Natural Science Foundation of China (Grant No. 2017CFB373).

412

413 References

- 414 Abdoun T, Dobry R, O'Rourke T, Goh S H (2003) Pile response to lateral spreads: Centrifuge
415 modeling. *Journal of Geotechnical and Geoenvironmental Engineering* 129(10): 869–878
- 416 Al-Defae AH, Caucis K, Knappett JA (2013) Aftershocks and the whole-life seismic performance of
417 granular slopes. *Géotechnique* 63(14): 1230–1244
- 418 Al-Defae AH, Knappett JA (2014) Centrifuge modeling of the seismic performance of pile-reinforced
419 slopes. *Journal of Geotechnical and Geoenvironmental Engineering* 140(6): 04014014
- 420 Al-Defae AH, Knappett JA (2015) Newmark sliding block model for pile-reinforced slopes under
421 earthquake loading. *Soil Dynamics and Earthquake Engineering* 75: 265–278
- 422 Bathe K J (1982) *Finite element analysis in engineering analysis*. Prentice-Hall, New Jersey
- 423 Brandenburg S J, Boulanger R W, Kutter B L, Chang D (2005) Behavior of pile foundations in laterally
424 spreading ground during centrifuge tests. *Journal of Geotechnical and Geoenvironmental*
425 *Engineering* 131(11): 1378–1391
- 426 Bonilia L F (2002) Borehole response studies at the Garner Valley Downhole Array, Southern
427 California. *Bulletin of the Seismological Society of America* 92(8): 3165–3179
- 428 Bourdeau C, Havenith H B (2008) Site effects modelling applied to the slope affected by the Suusamy
429 earthquake (Kyrgyzstan, 1992). *Engineering Geology* 97(3–4): 126–145
- 430 Cao ZZ, Youd TL, Yuan XM (2011) Gravelly soils that liquefied during 2008 Wenchuan, China
431 earthquake, Ms=8.0. *Soil Dynamics and Earthquake Engineering* 31(8): 1132–1143
- 432 Carder DR, Temporal J (2000) A review of the use of spaced piles to stabilise embankment and cutting
433 slopes. TRL Report 466, Transportation Research Laboratory, Berkshire, UK
- 434 Chen YM, Li JC, Yang CB, Zhu B, Zhan LT (2017) Centrifuge modeling of municipal solid waste
435 landfill failures induced by rising water levels. *Canadian Geotechnical Journal* 54(12): 1739–1751
- 436 Chigira M, Wu XY, Inokuchi T, Wang GH (2010) Landslides induced by the 2008 Wenchuan

437 earthquake, Sichuan, China. *Geomorphology* 118: 225–238

438 Del Gaudio V, Wasowski J (2011) Advances and problems in understanding the seismic response of
439 potentially unstable slopes. *Engineering Geology* 122(1–2): 73–83

440 Ding Y, Dang C, Yuan GX, Wang QC (2012) Characteristics and remediation of a landslide complex
441 triggered by the 2008 Wenchuan, China earthquake—case from Yingxiu near the earthquake
442 epicenter. *Environ Earth Sci* 67:161–173

443 Ellis EA, Durrani IK, Reddish DJ (2010) Numerical modelling of discrete pile rows for slope stability
444 and generic guidance for design. *Géotechnique* 60(3): 185–195

445 Erfani JA, Liang RY, Li L, Liu HL (2014) Yield acceleration and permanent displacement of a slope
446 reinforced with a row of drilled shafts. *Soil Dynamics and Earthquake Engineering* 57: 68–77.
447 doi:10.1016/j.soildyn.2013. 10.011

448 Garala KT, Madabhushi SPG (2019) Seismic behaviour of soft clay and its influence on the response of
449 friction pile foundations. *Bulletin of Earthquake Engineering* 17:1919–1939.
450 <https://doi.org/10.1007/s10518-018-0508-4>

451 GB (2010) Code for seismic design of buildings, 50011-2010. China Building Industry Press, Beijing
452 (in Chinese)

453 Gischig V S, Eberhardt E, Moore J R, Hungr O (2015) On the seismic response of deep seated rock
454 slope instabilities—insights from numerical modeling. *Engineering Geology* 193: 1–18

455 Huang RQ, Li WL (2009) Analysis of the geo-hazards triggered by the 12 May 2008 Wenchuan
456 Earthquake, China. *Bull Eng Geol Environ* 68: 363–371

457 Huang Y, Xu X, Liu JJ, Mao W (2020) Centrifuge modeling of seismic response and failure mode of a
458 slope reinforced by a pile-anchor structure. *Soil Dynamics and Earthquake Engineering* 131: 1–11.
459 <https://doi.org/10.1016/j.soildyn.2020.106037>

460 Kanagasabai S, Smethurst JA, Powrie W (2011) Three-dimensional numerical modelling of discrete
461 piles used to stabilize landslides. *Canadian Geotechnical Journal* 48(9): 1393–1411. doi:
462 10.1139/t11-046

463 Knappett J A, Madabhushi S P G (2009) Influence of axial load on lateral pile response in liquefiable
464 soils. Part I: physical modelling. *Géotechnique*, 59(7), 571–581. doi:10.1680/geot.8.009.3749

465 Kourkoulis R, Gelagoti F, Anastasopoulos I, Gazetas G (2011) Slope stabilizing piles and pile-groups:
466 Parametric study and design insights. *Journal of Geotechnical and Geoenvironmental Engineering*
467 137(7): 663–677. doi:10.1061/(asce)gt.1943-5606.0000479

468 Kourkoulis R, Gelagoti F, Anastasopoulos I, Gazetas G (2012) Hybrid method for analysis and design
469 of slope stabilizing piles. *Journal of Geotechnical and Geoenvironmental Engineering* 138(1): 1–14

470 Li CD, Wu J, Tang HM, Hu XL, Liu XW, Wang CQ, Liu T, Zhang YQ (2016) Model testing of the
471 response of stabilizing piles in landslides with upper hard and lower weak bedrock. *Engineering*
472 *Geology* 204: 65–76

473 Li X, Pei X, Gutierrez M, He SM (2012) Optimal location of piles in slope stabilization by limit
474 analysis. *Acta Geotechnica* 7(3): 253–259

475 Li Z, Escoffier S, Kotronis P (2016) Centrifuge modeling of batter pile foundations under sinusoidal
476 dynamic excitation. *Bulletin of Earthquake Engineering* 14(3): 673–697

477 Lirer S (2012) Landslide stabilizing piles: Experimental evidences and numerical interpretation.
478 *Engineering Geology* 149-150: 70–77

479 Ma N, Wu HG, Ma HM, Wu XY, Wang GH (2019) Examining dynamic soil pressures and the
480 effectiveness of different pile structures inside reinforced slopes using shaking table tests. *Soil*

481 Dynamics and Earthquake Engineering 116: 293–303

482 Massey C, Della Pasqua F, Holden C, Kaiser A, Richards L, Wartman J, McSaveney MJ, Archibald G,
483 Yetton M, Janku L (2017) Rock slope response to strong earthquake shaking. *Landslides* 14(1):
484 249–268. doi:10.1007/s10346-016-0684-8

485 Moore JR, Gischig VS, Burjanek J, Loew S, Fah D (2011) Site effects in unstable rock slopes: dynamic
486 behavior of the Randa instability (Switzerland). *Bulletin Seismological Society America* 101(6):
487 3110–3116

488 Newmark N M (1965) Effects of earthquakes on dams and embankments. *Géotechnique* 15(2):
489 139–160

490 Ou J F, Luo Y H, Wang Y S, Zhu XM, Zhang YY (2019) Analysis of response characteristics of slope
491 ground motion based on environmental noise and seismic data: A case study of Lushan Renjia slope.
492 *Journal of Mountain Science* 37(3) : 382–391. (in Chinese)

493 PLAXIS 2D (2015) Reference manual, Last version 2015.2.19890.4979. Delft, Netherlands: Delft
494 University of Technology

495 Sharafi H, Shams Maleki Y (2019) Evaluation of the lateral displacements of a sandy slope reinforced
496 by a row of floating piles: A numerical-experimental approach. *Soil Dynamics and Earthquake*
497 *Engineering* 122: 148–170

498 Smethurst JA, Powrie W (2007) Monitoring and analysis of the bending behaviour of discrete piles
499 used to stabilise a railway embankment. *Géotechnique* 57(8): 663–677

500 Spence R (2015) The full-scale laboratory: the practice of post-earthquake reconnaissance missions and
501 their contribution to earthquake engineering. *Bull Earthquake Eng* 13:1581–1585.
502 doi:10.1007/s10518-015-9751-0

503 Strenk P M, Wartman J (2011) Uncertainty in seismic slope deformation model predictions.
504 *Engineering Geology* 122(1–2): 61–72

505 Sun ZL, Kong LW, Guo AG, Xu GF, Bai Wei (2019) Experimental and numerical investigations of the
506 seismic response of a rock–soil mixture deposit slope. *Environ Earth Sci* 78(24): 716. doi:10.1007/
507 s12665-019-8717-y

508 Wang KL, Lin ML (2011) Initiation and displacement of landslide induced by earthquake—A study of
509 shaking table model slope test. *Engineering Geology* 122(1–2):106–114

510 Wang LP, Zhang G (2014) Centrifuge model test study on pile reinforcement behavior of cohesive soil
511 slopes under earthquake conditions. *Landslides* 11(2): 213–223

512 Won J, You K, Jeong S, Kim S (2005) Coupled effects in stability analysis of pile-slope systems.
513 *Comput Geotech* 32(4): 304–315

514 Wu Y, He SM, Li XP (2009) Failure mechanism of anti-slide pile under seismic wave. *Journal of*
515 *Sichuan University: Engineering Science* 41(3): 284–288. (in Chinese)

516 Yin YP, Wang FW, Sun P (2009) Landslide hazards triggered by the 2008 Wenchuan earthquake,
517 Sichuan, China. *Landslides* 6(2):139–152

518 Yu Y, Deng L, Sun X, Lü H (2010) Centrifuge modeling of dynamic behavior of pile-reinforced slopes
519 during earthquakes. *Journal of Central South University of Technology* 17(5):1070–1078.
520 doi:10.1007/s11771-010-0599-9

521 Zhou YG, Sun ZB, Chen YM (2018) Zhejiang University benchmark centrifuge test for
522 LEAP-GWU-2015 and liquefaction responses of a sloping ground. *Soil Dynamics and Earthquake*
523 *Engineering* 113: 698–713

Figures

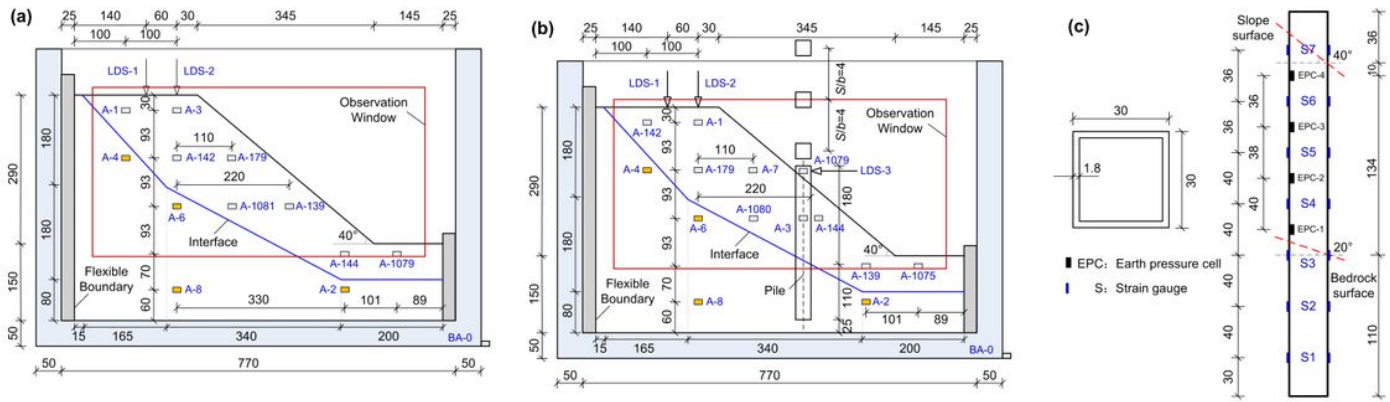


Figure 1

Layout of model slope and instrumentation at model-scale. a 1#model. b 2#model. c Layout of earth pressure cells and strain gauges on a model pile (unit: mm)

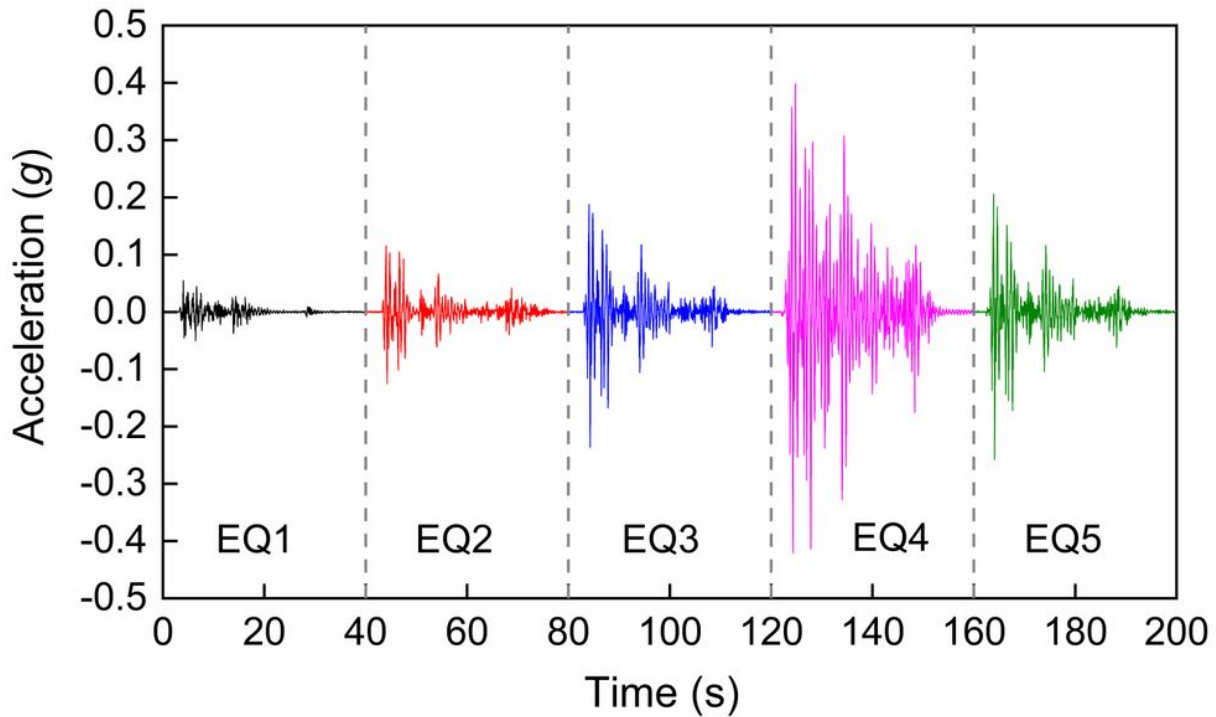


Figure 2

Time histories of input motions at instrument BA-0

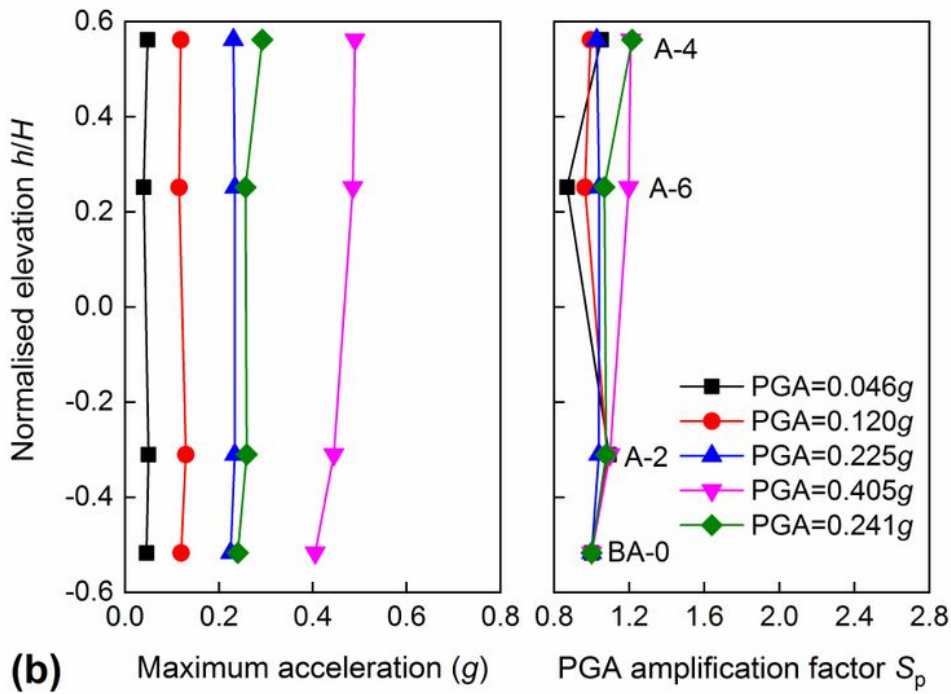
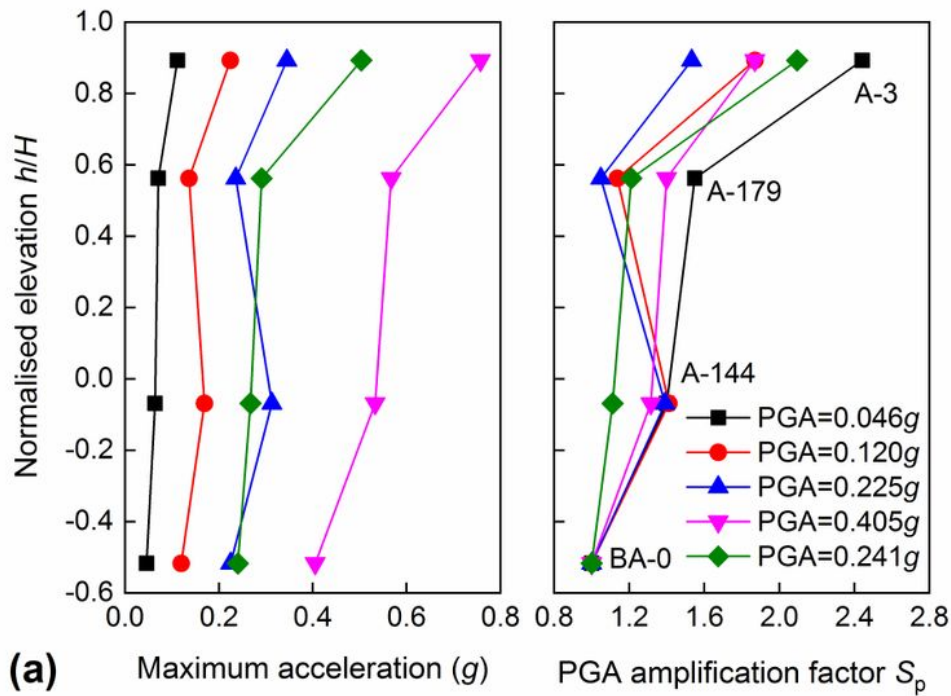


Figure 3

Maximum acceleration distributions along the normalised slope elevation in the 1#model in centrifuge tests. a Deposit surface. b Bedrock surface

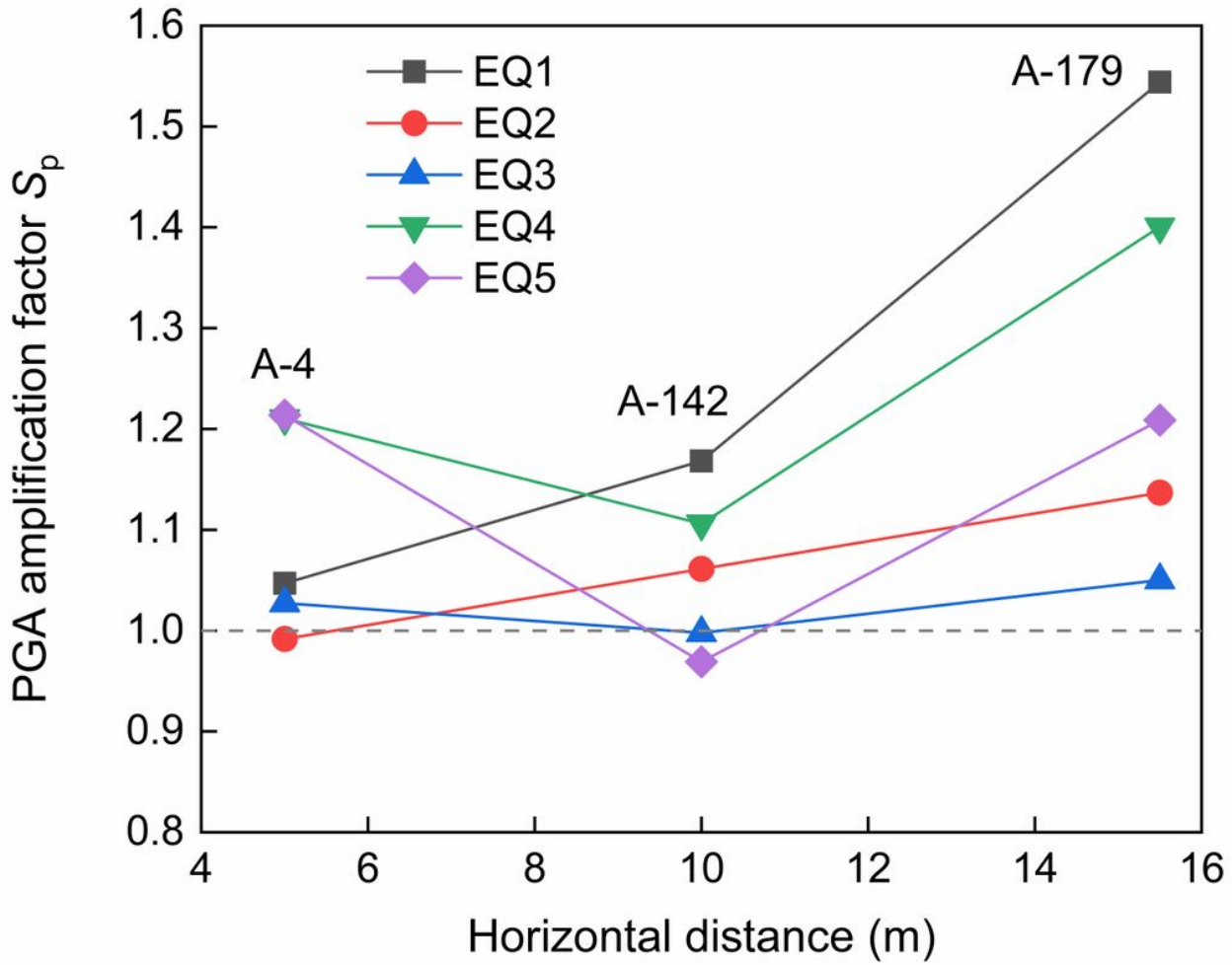


Figure 4

The horizontal acceleration amplification factor distribution from the inside of the slope to its surface at a height of 15.8m in the 1#model in centrifuge tests

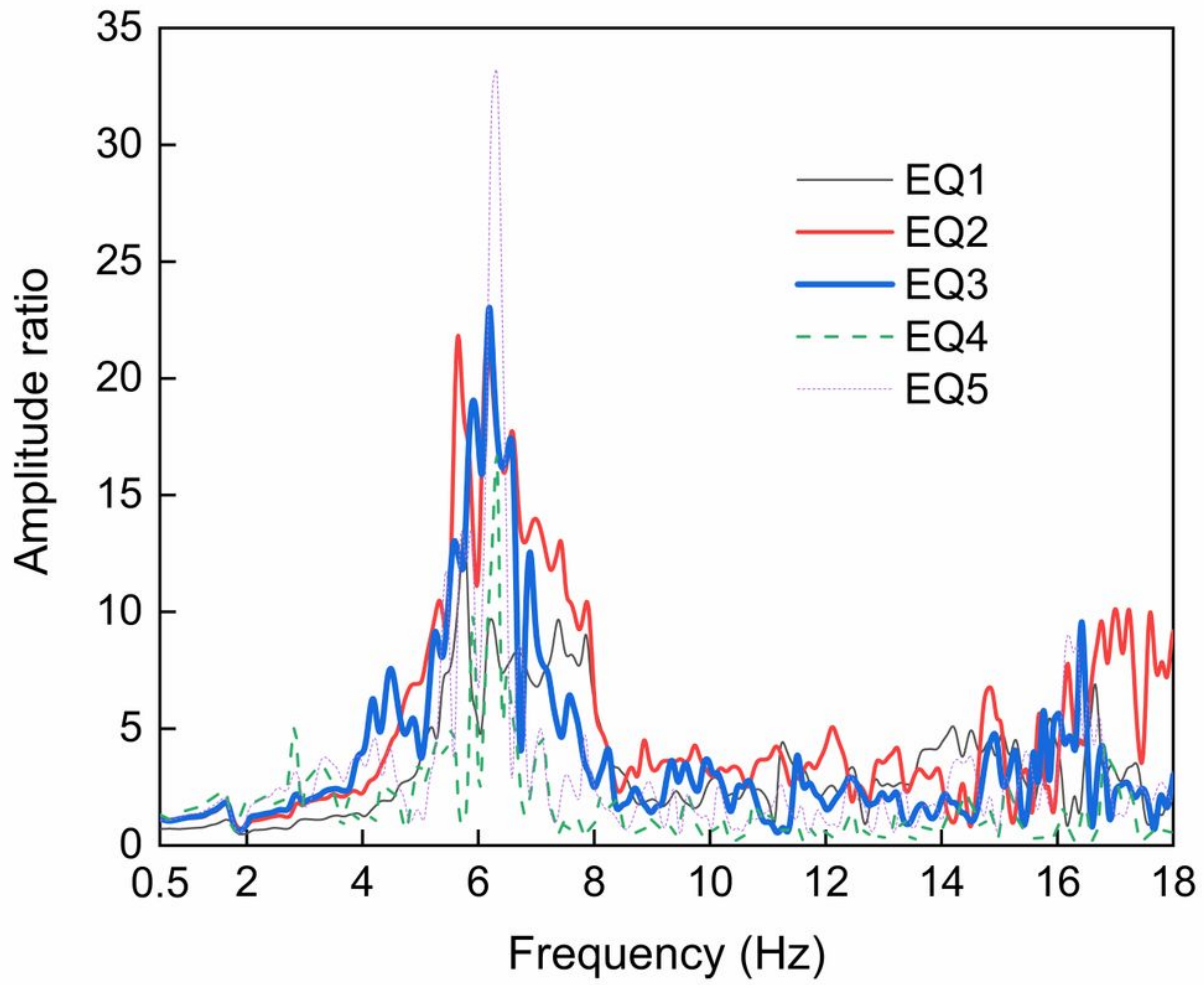


Figure 5

The amplitude ratios of the transfer function of the acceleration measured at A-3(slope crest) and A-0 (bottom of the model box) in the 1#model during centrifuge testing

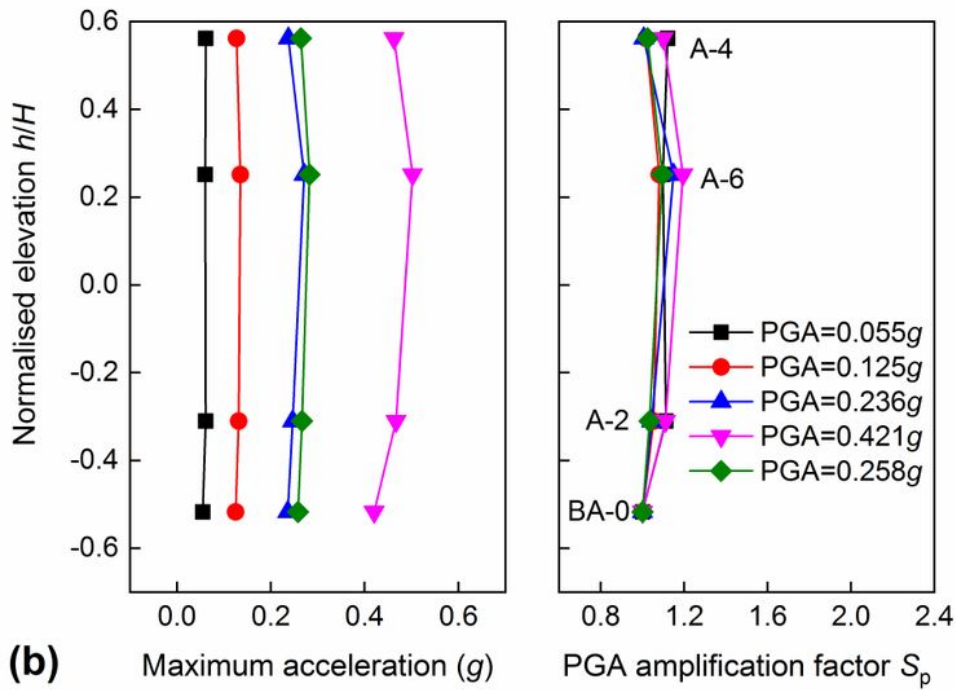
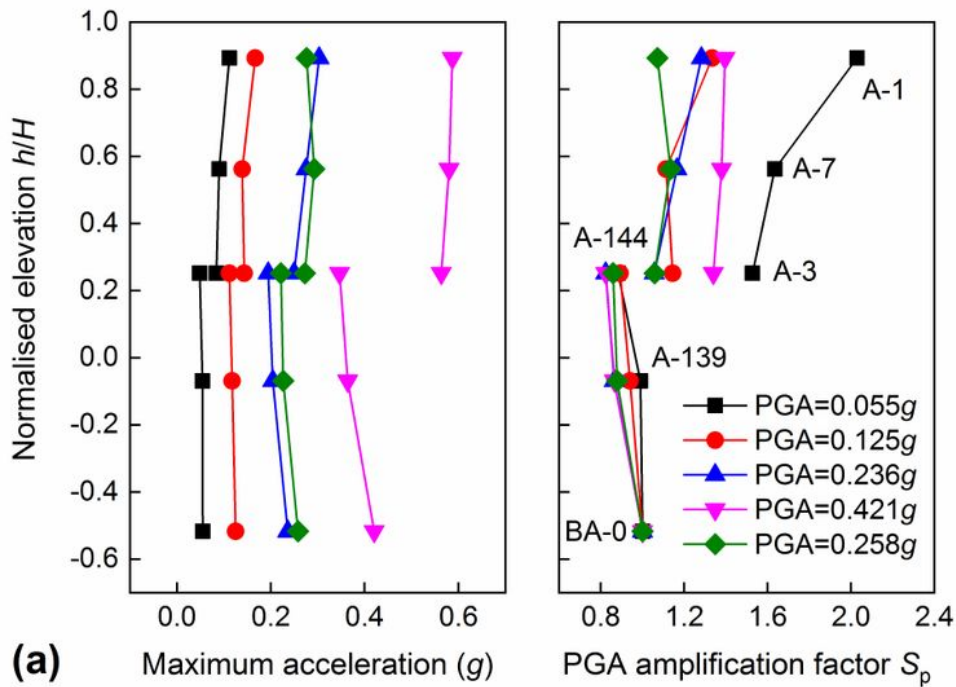


Figure 6

Maximum acceleration distributions along the normalised slope elevation in the 2#model in centrifuge tests. a Deposit surface. b Bedrock surface

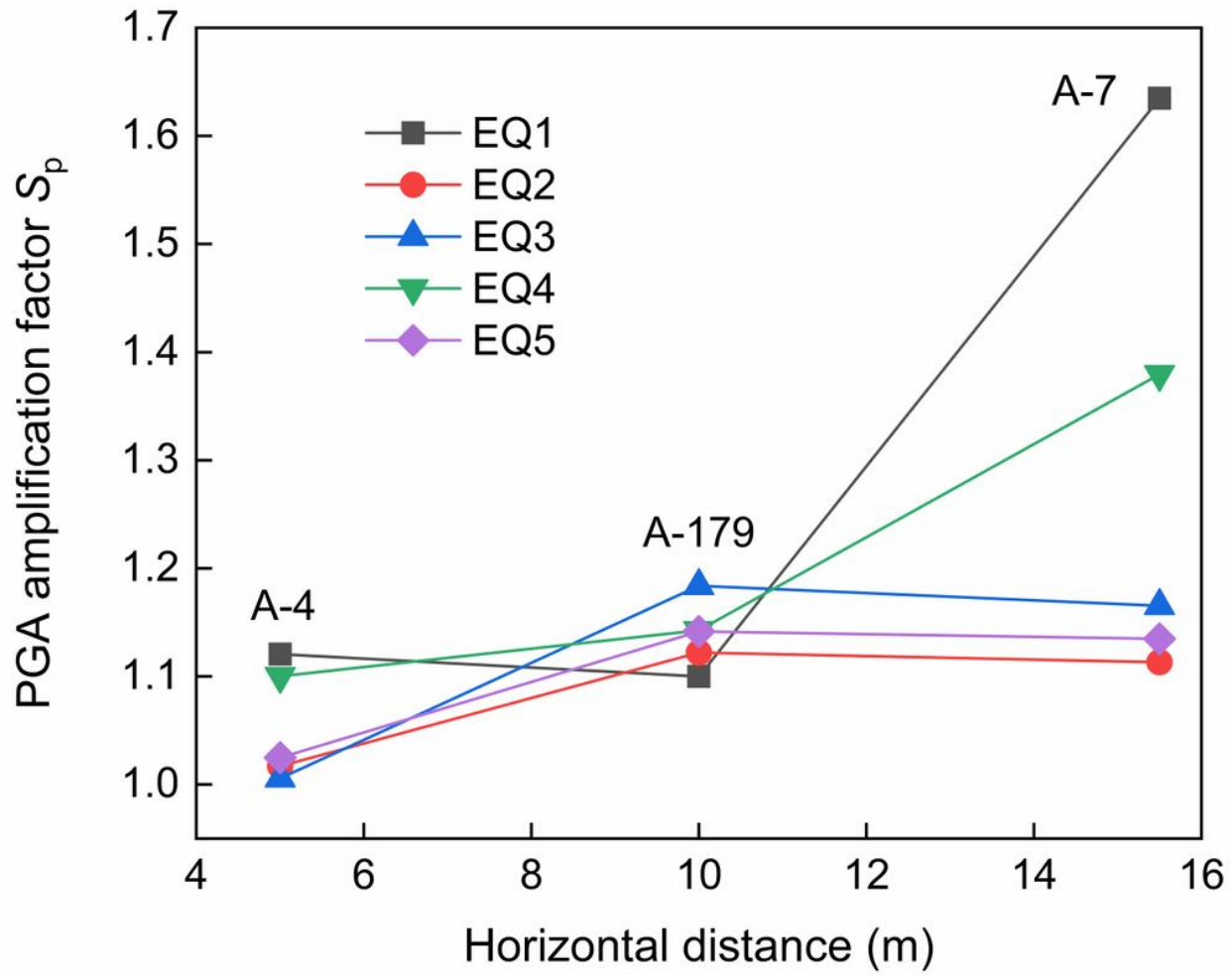


Figure 7

The horizontal acceleration amplification factor distribution from the inside of the slope to the surface of the slope at a height of 15.8m in the 2#model in centrifuge tests

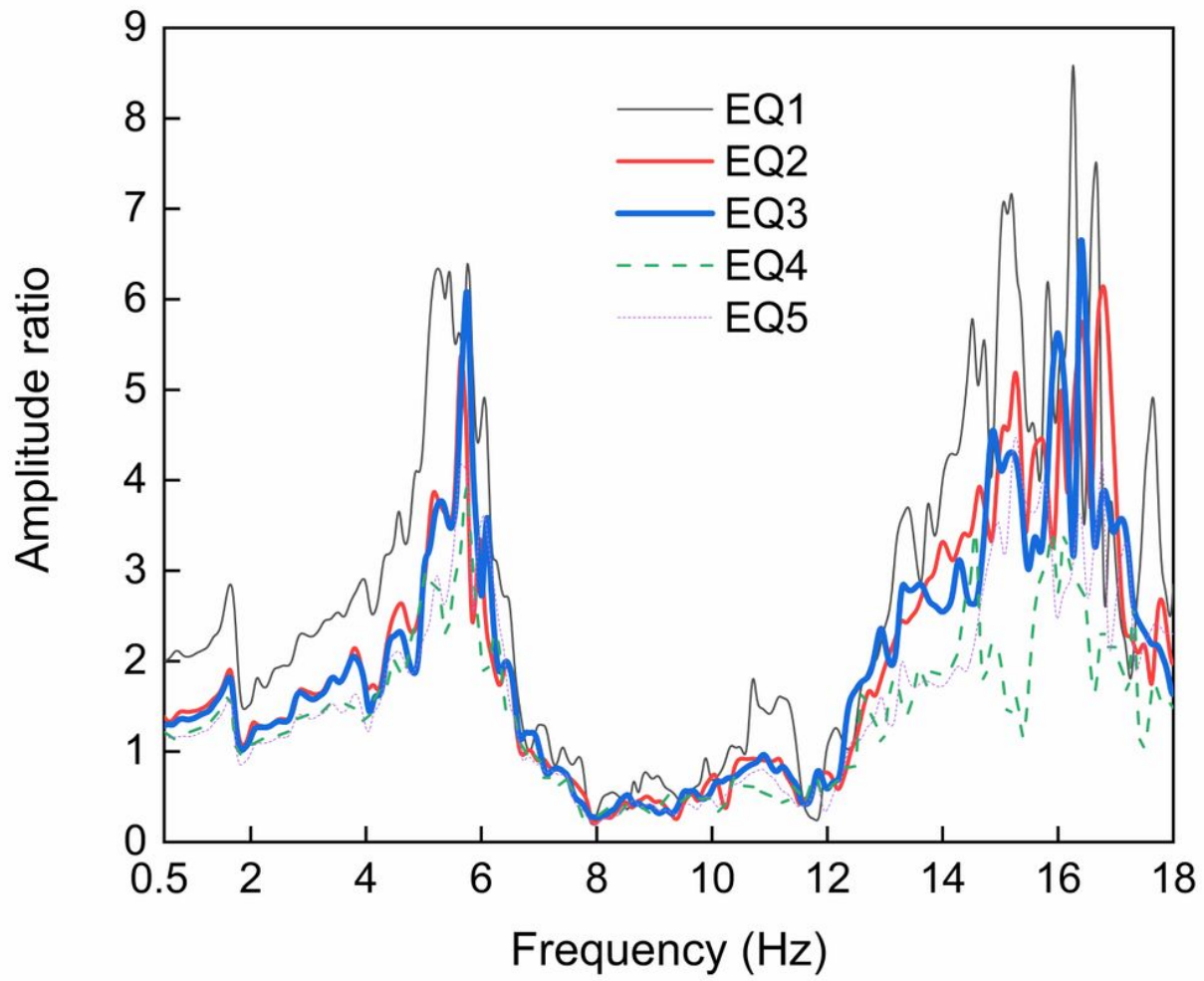


Figure 8

The amplitude ratios of the transfer function of the acceleration measured at A-1 (slope crest) and A-0 (bottom of the model box) in the 2#model during centrifuge testing

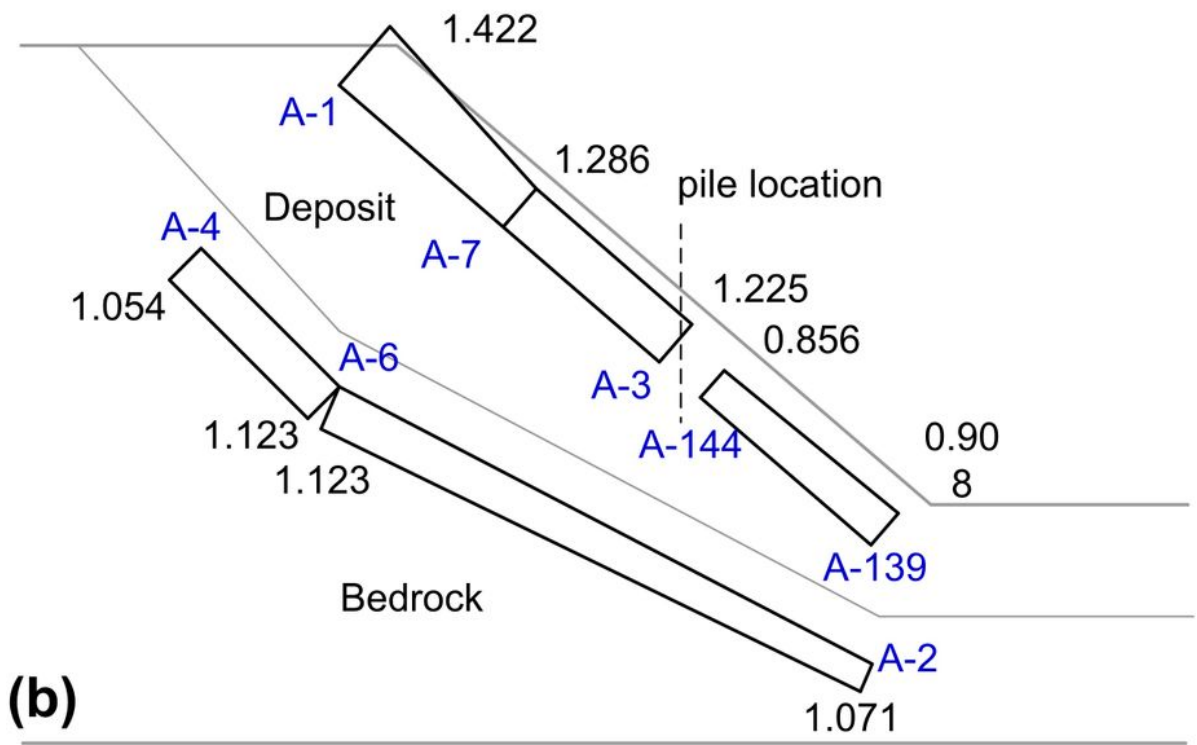
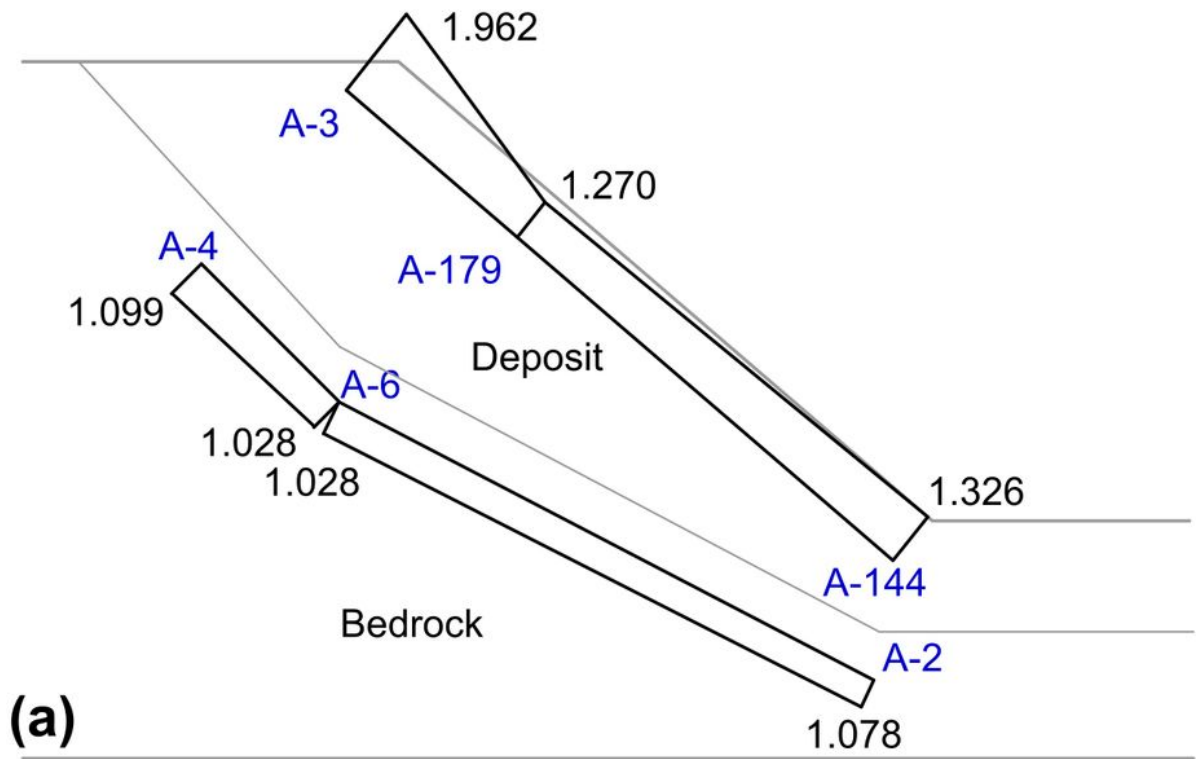


Figure 9

Average horizontal PGA amplification factor distribution in the underlying bedrock deposit slope in centrifuge tests. a 1#model. b 2#model

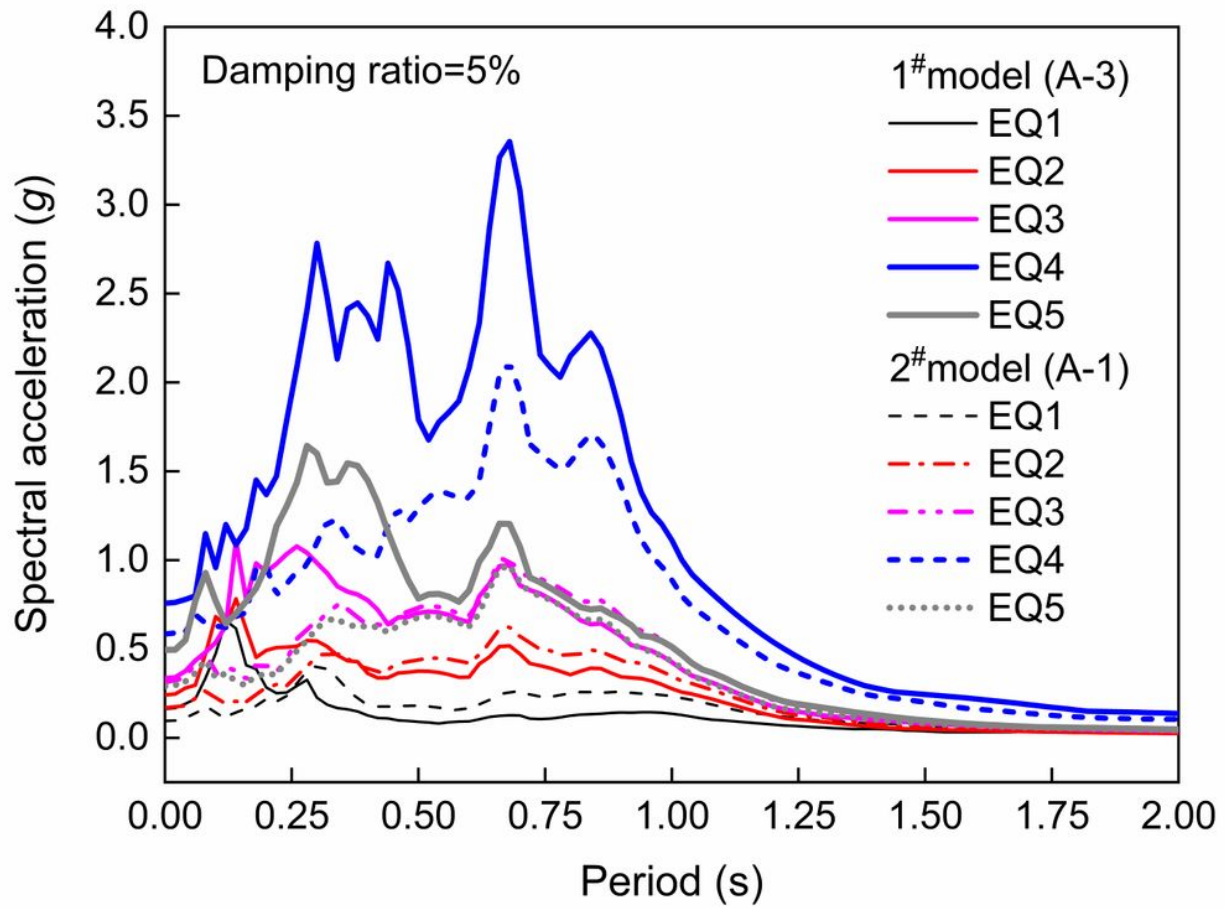
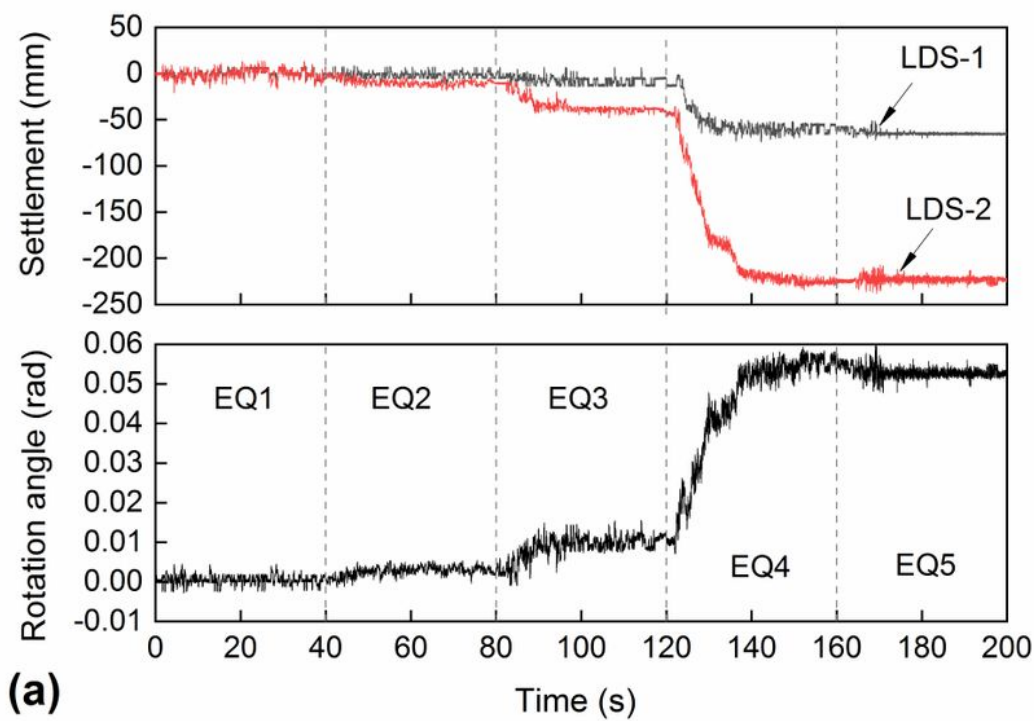
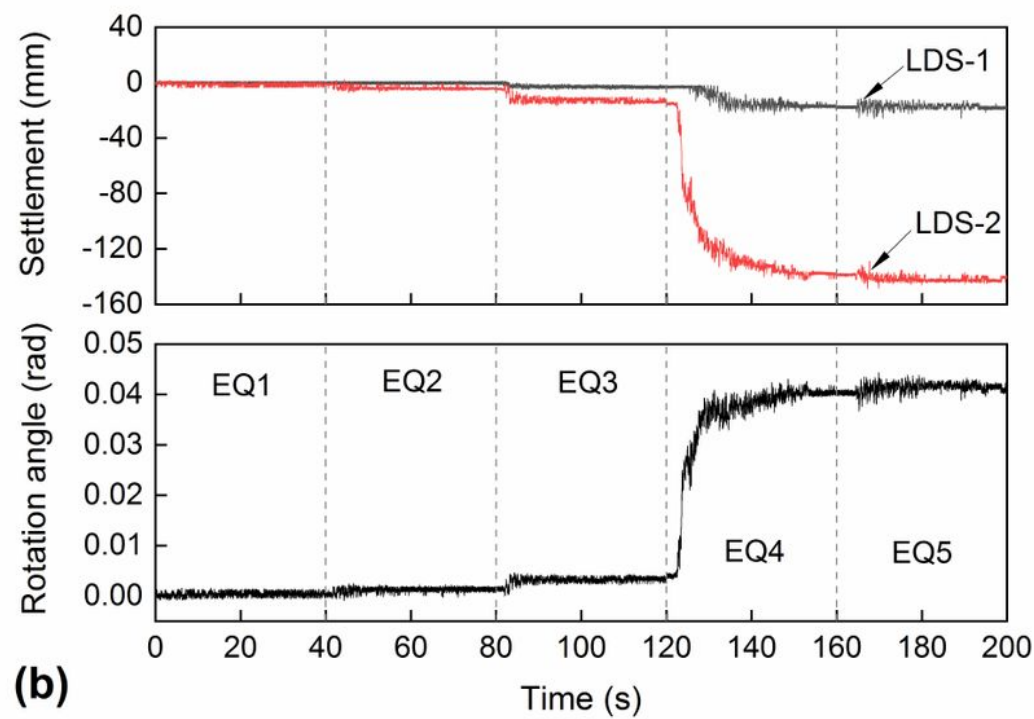


Figure 10

Response spectral accelerations of the slope crest (5% damping ratio)



(a)



(b)

Figure 11

Crest settlements and crest rotation angle under seismic excitation. a 1#model. b 2#model

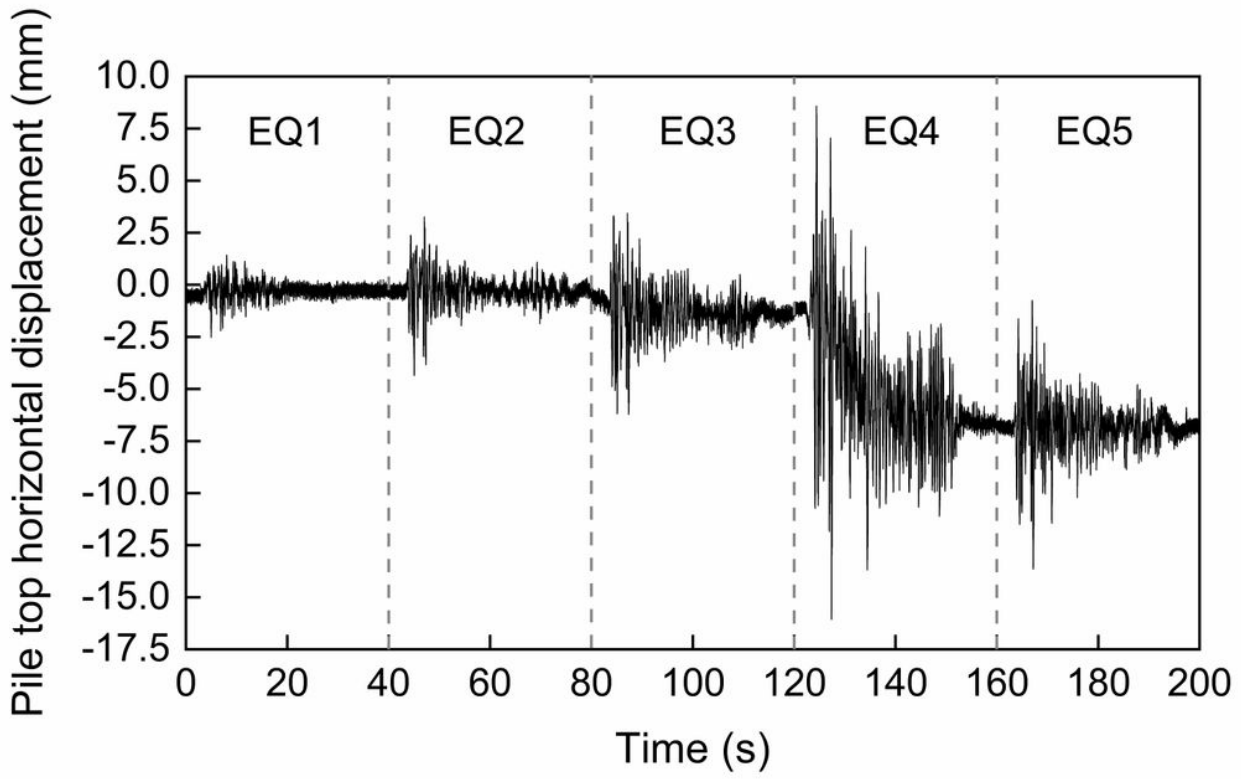


Figure 12

Pile top horizontal displacement under seismic excitations in the 2#model

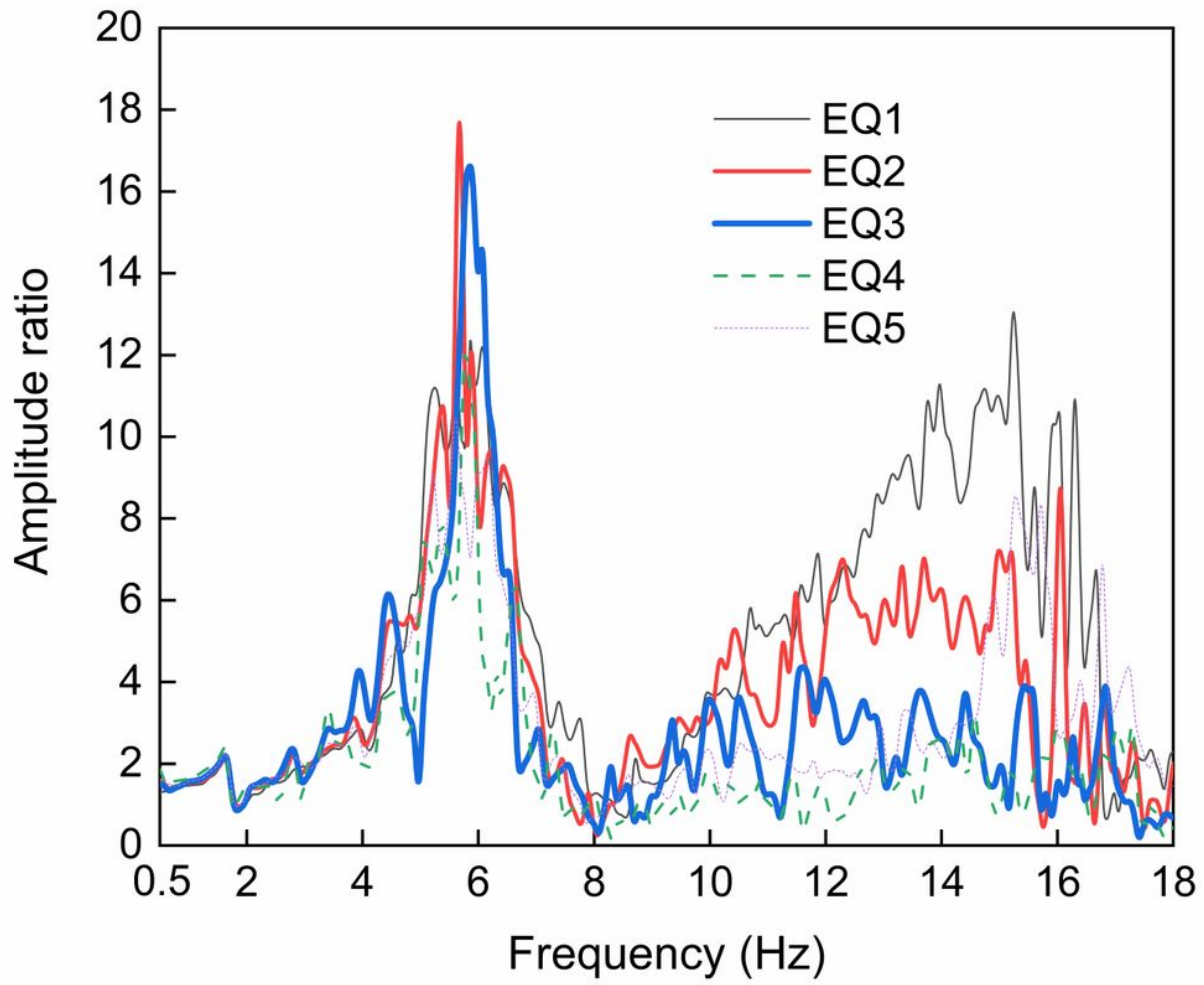


Figure 13

The amplitude ratios of the transfer function of the acceleration measured at A-1079 (pile top) and A-0 (bottom of the model box) in the 2#model during centrifuge testing

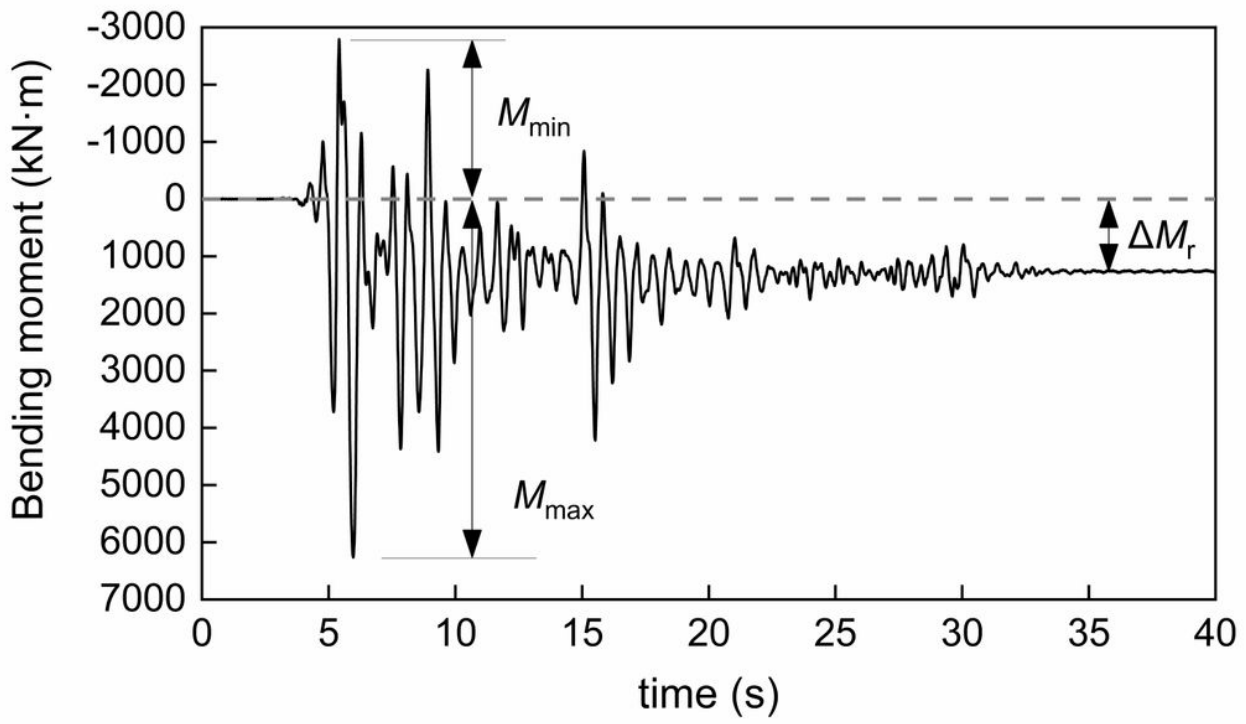


Figure 14

Typical response time-history curves of bending moments in the centrifuge test (EQ4, S3)

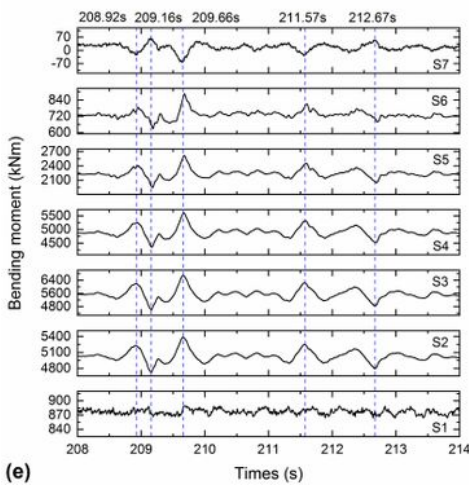
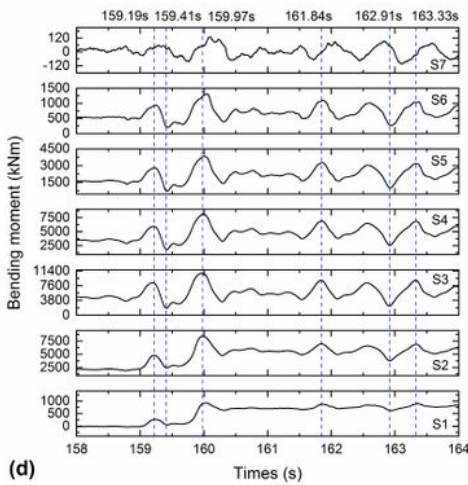
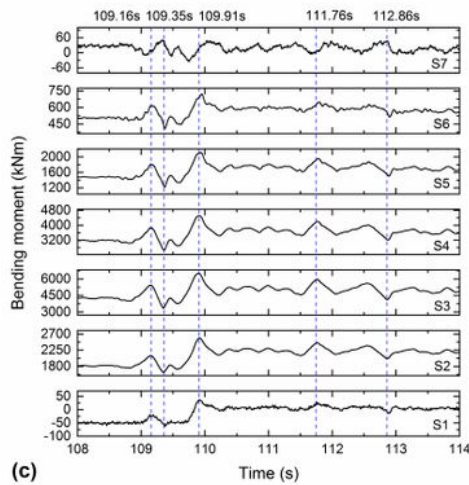
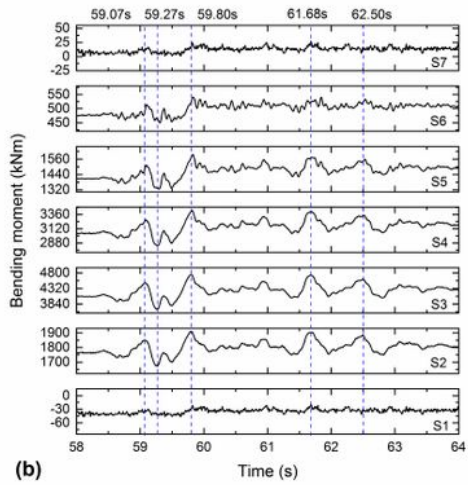
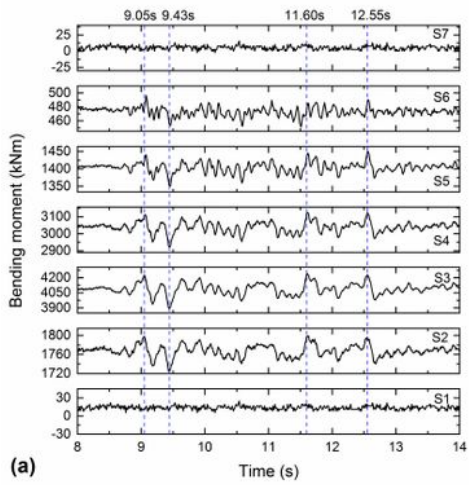


Figure 15

Time-history curves of bending moments in centrifuge tests. a EQ1. b EQ2. c EQ3. d EQ4. e EQ5

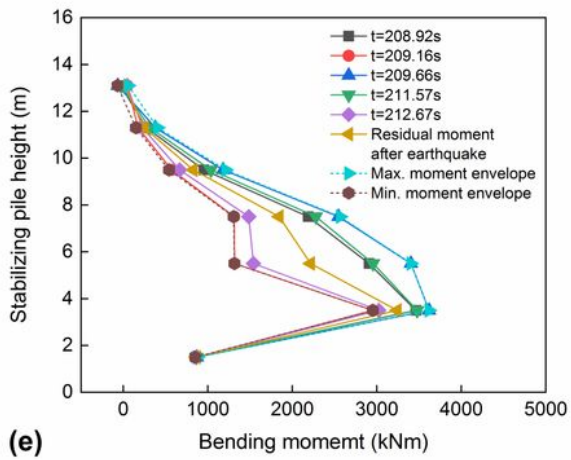
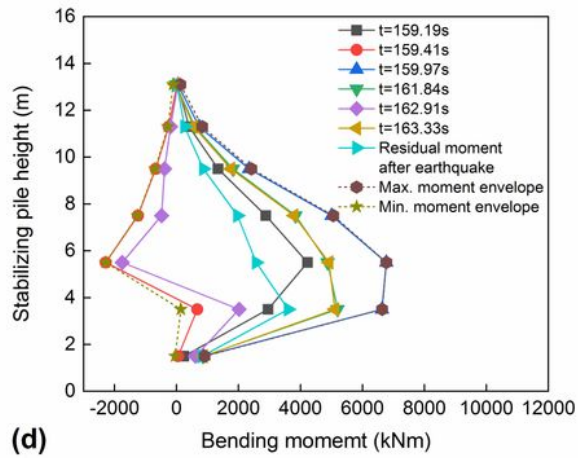
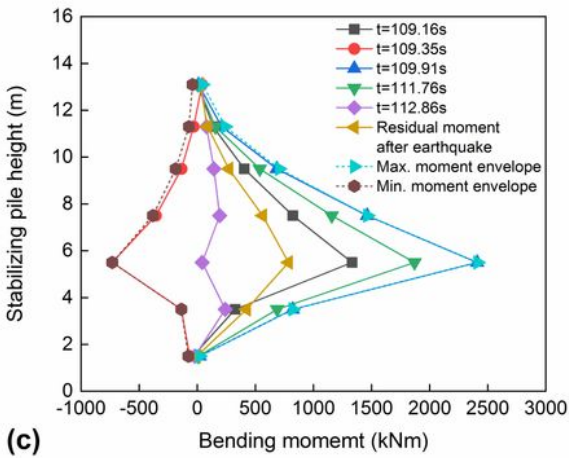
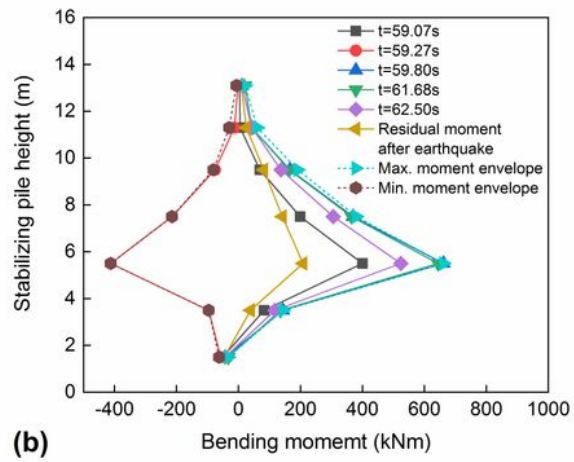
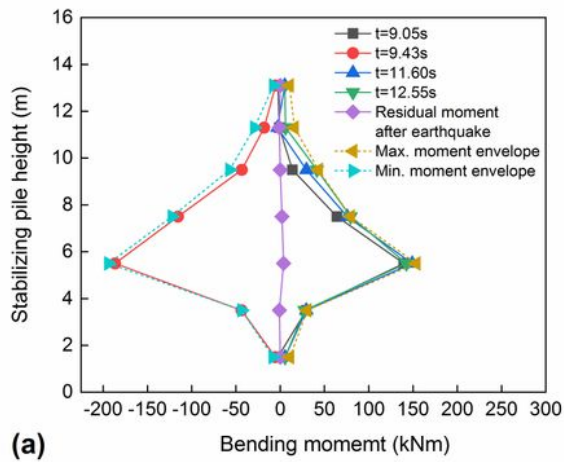


Figure 16

Maximum and minimum bending moment envelopes, residual bending moment after an earthquake, and the dynamic bending moment on a stabilising pile. a EQ1. b EQ2. c EQ3. d EQ4. e EQ5

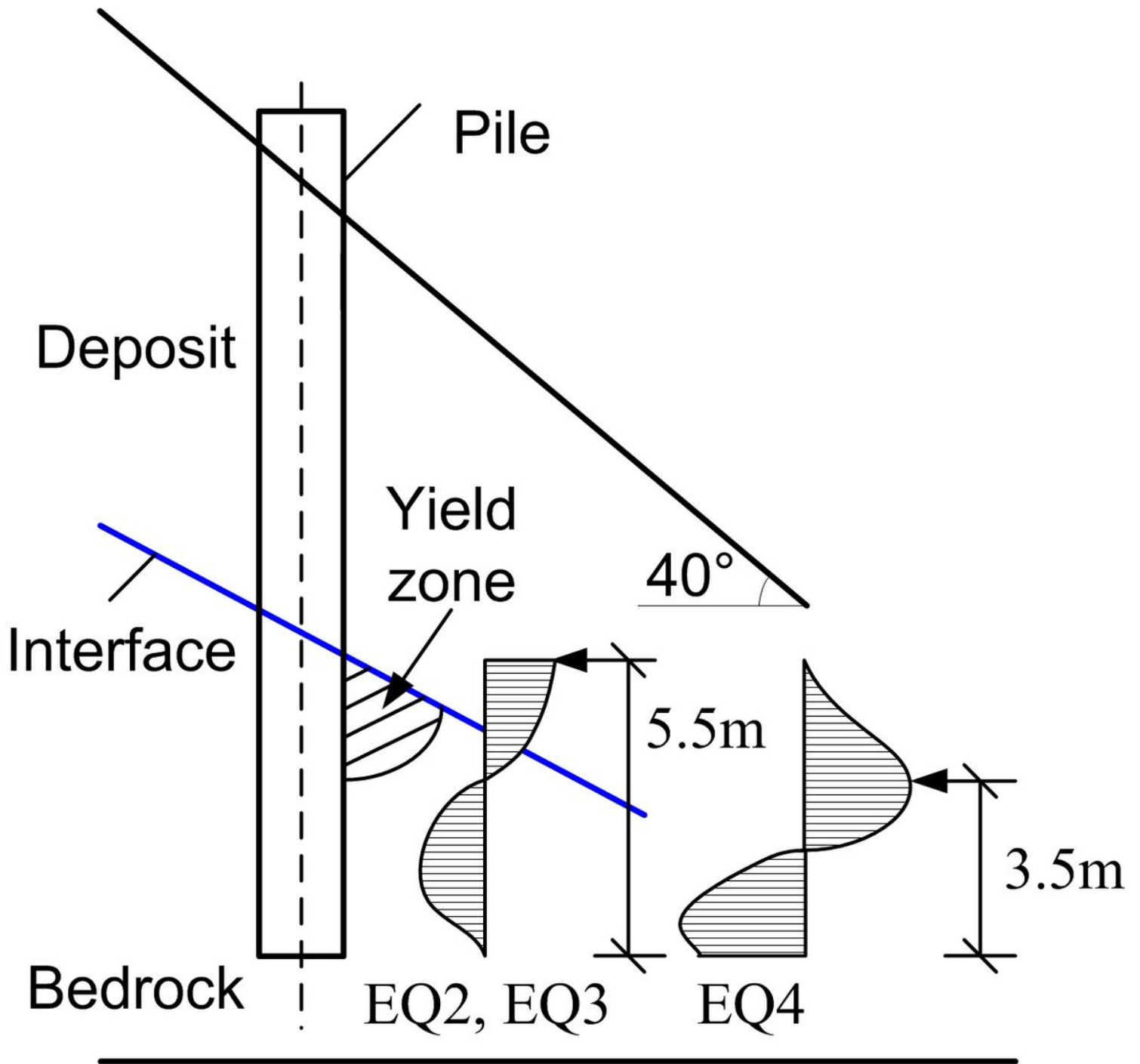


Figure 17

Schematic representation of the resistance exerted by a stabilising pile in the bedrock

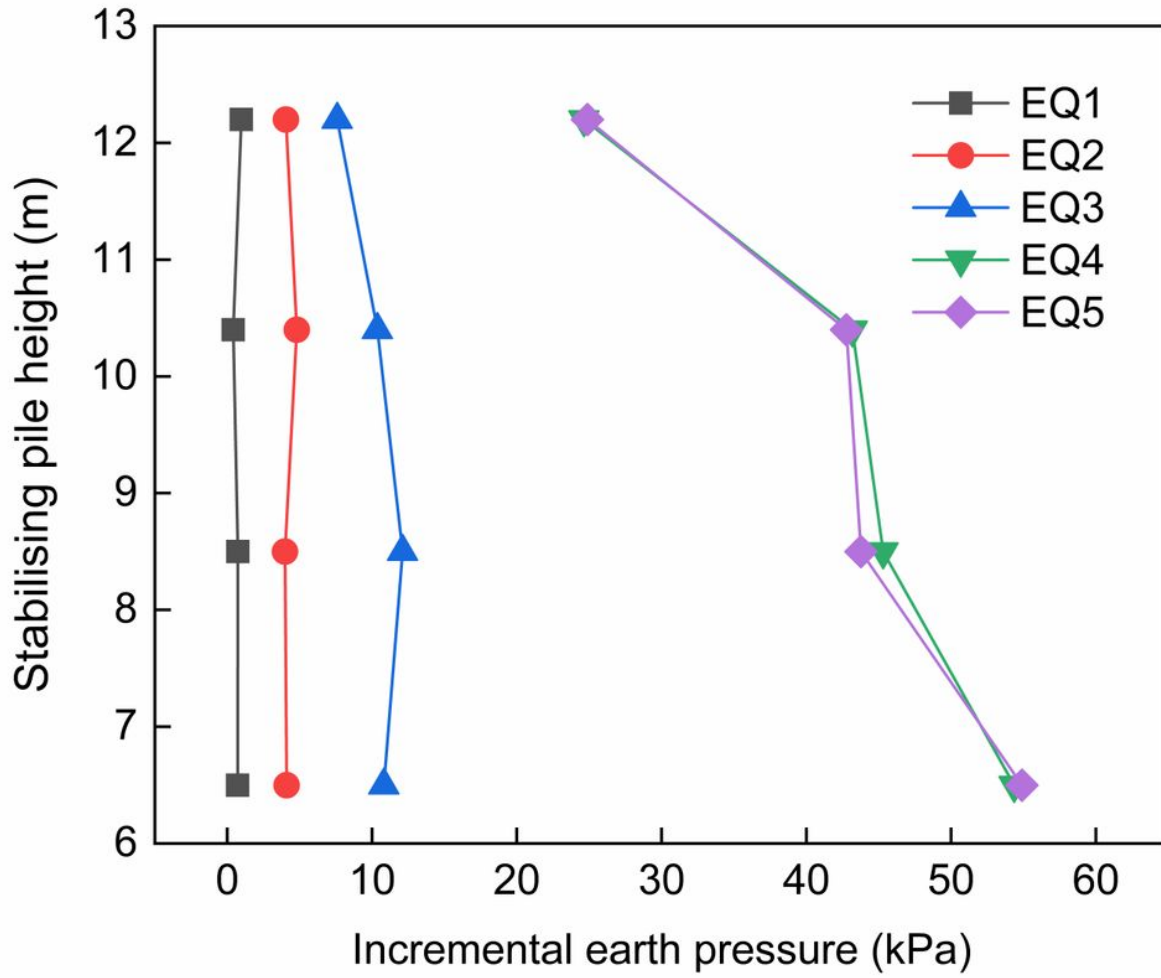


Figure 18

Incremental earth pressure measured by earth pressure cell after each shaking event

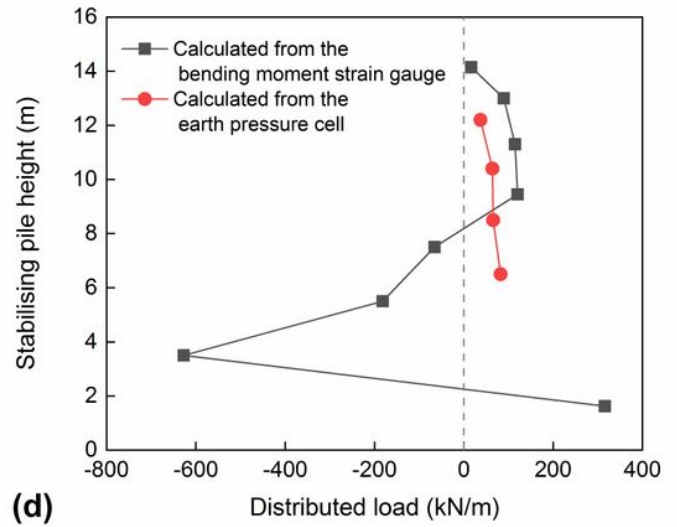
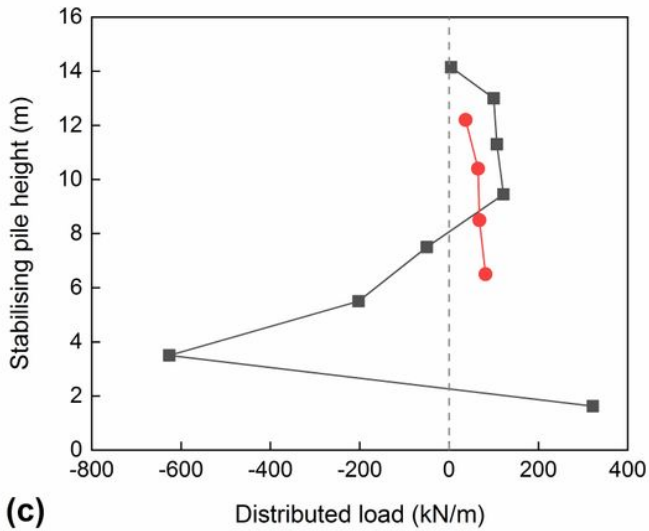
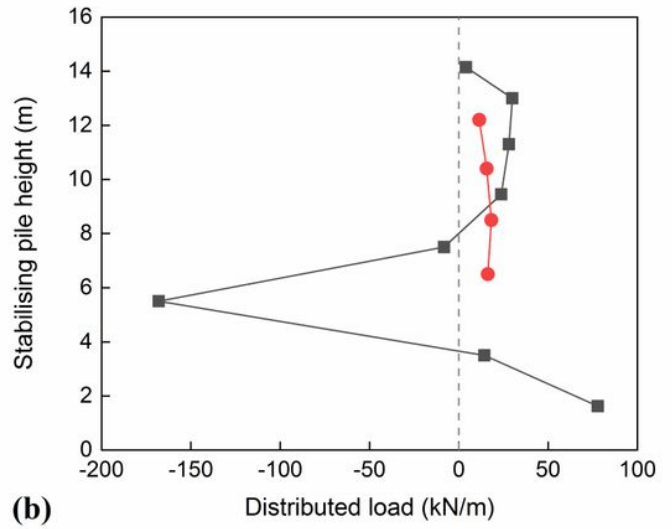
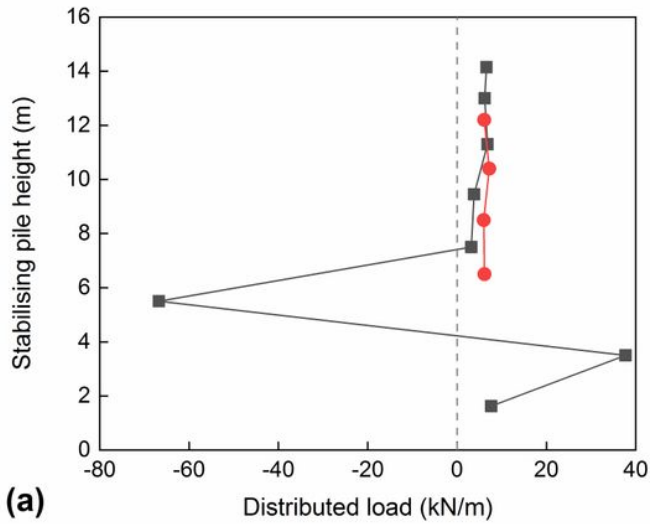


Figure 19

Comparison of distributed load increment obtained by moment strain gauge and earth pressure cell on a stabilising pile after each shaking event. a EQ2. b EQ3. c EQ4. d EQ5

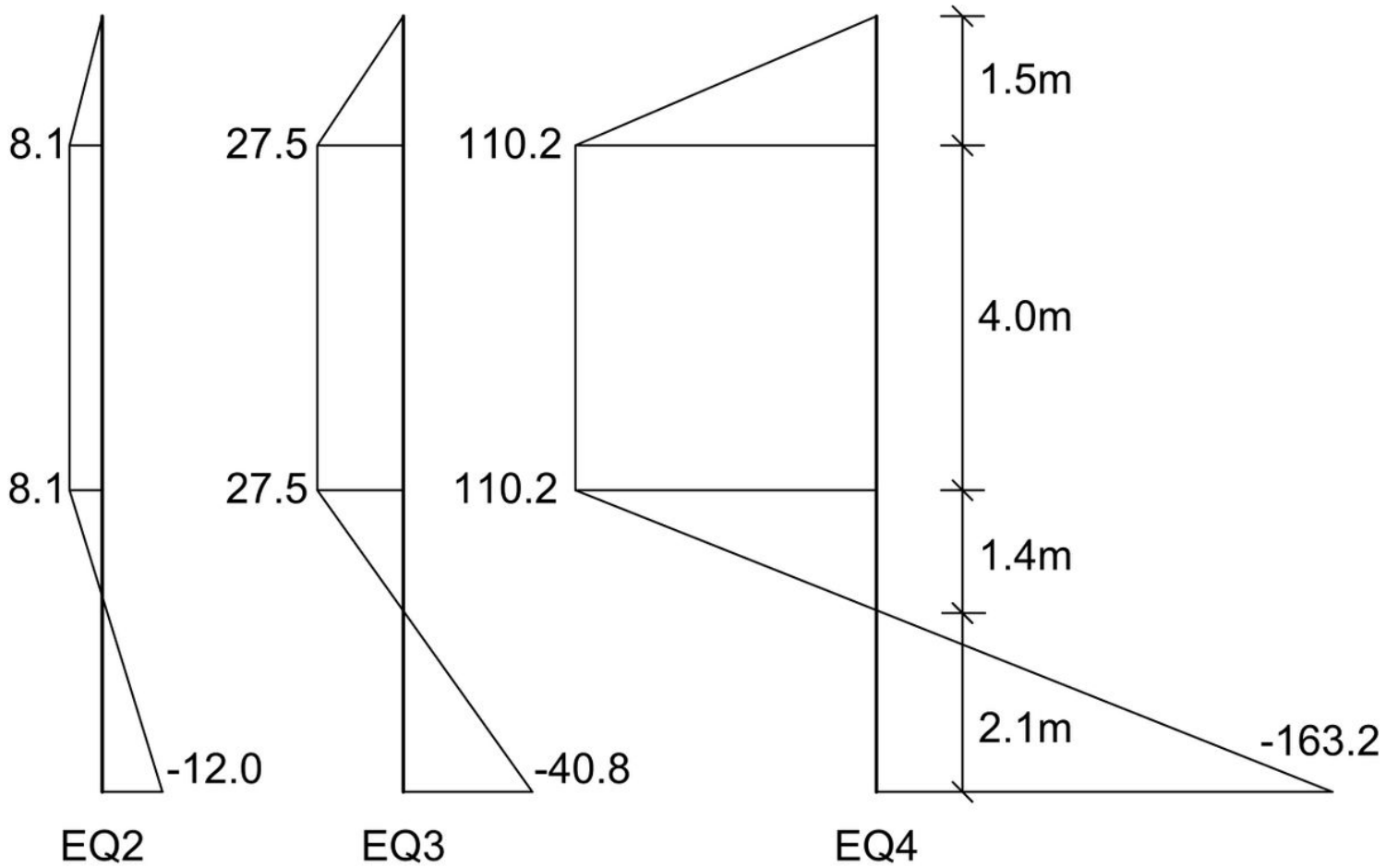


Figure 20

Simplified distributed load increment above the slip surface after each shaking event (unit: kN/m)

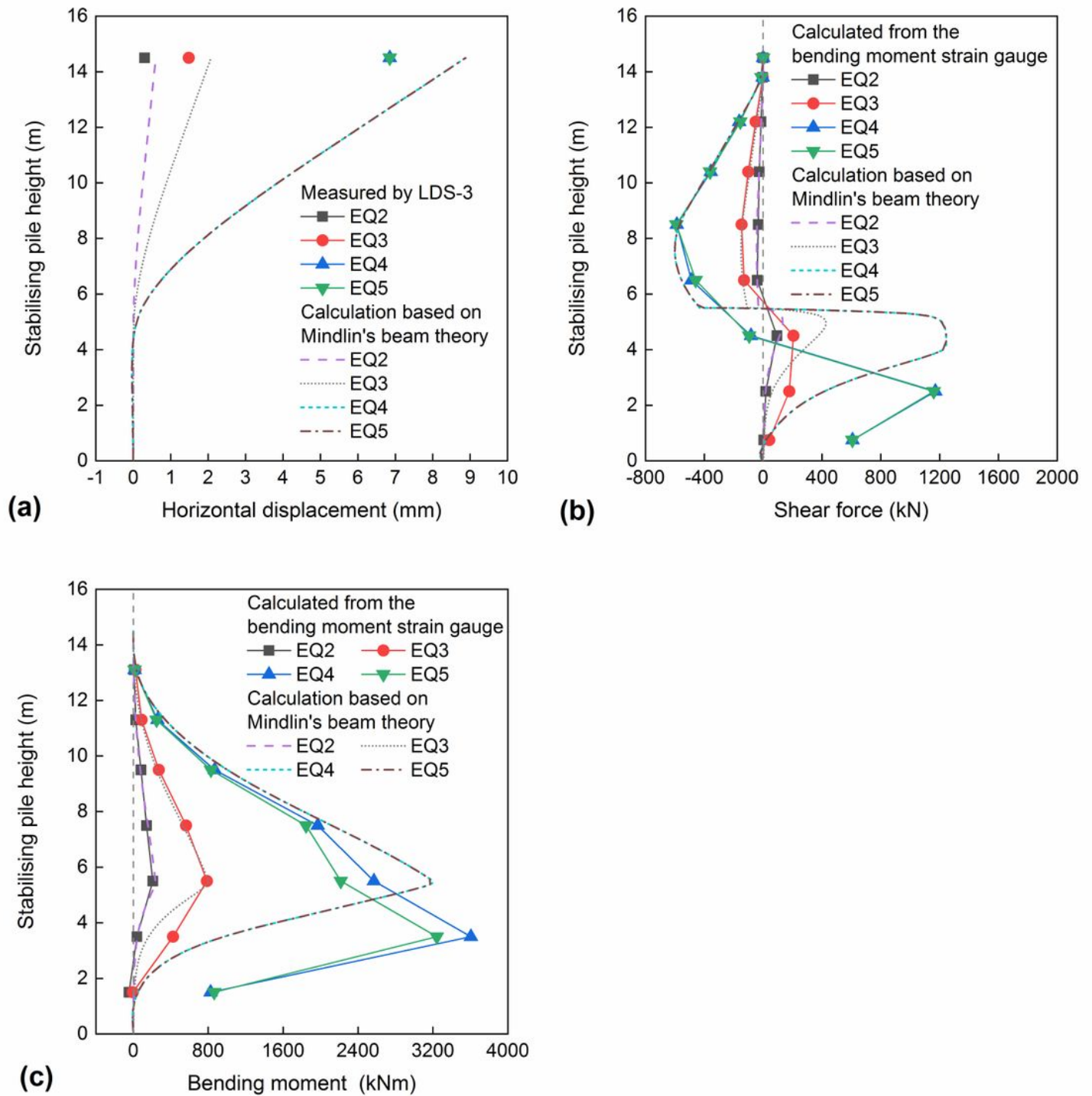


Figure 21

Comparison of the calculated results after test-measurement conversion and the calculated results based on Mindlin beam theory for a stabilising pile after each shaking event. a Horizontal displacement. b Shear force. c Bending moment